

UV Volumes for Real-time Rendering of Editable Free-view Human Performance

Yue Chen^{1*} Xuan Wang^{2,3*} Xingyu Chen¹ Qi Zhang³
 Xiaoyu Li³ Yu Guo^{1†} Jue Wang³ Fei Wang¹
¹Xi'an Jiaotong University ²Ant Group ³Tencent AI Lab

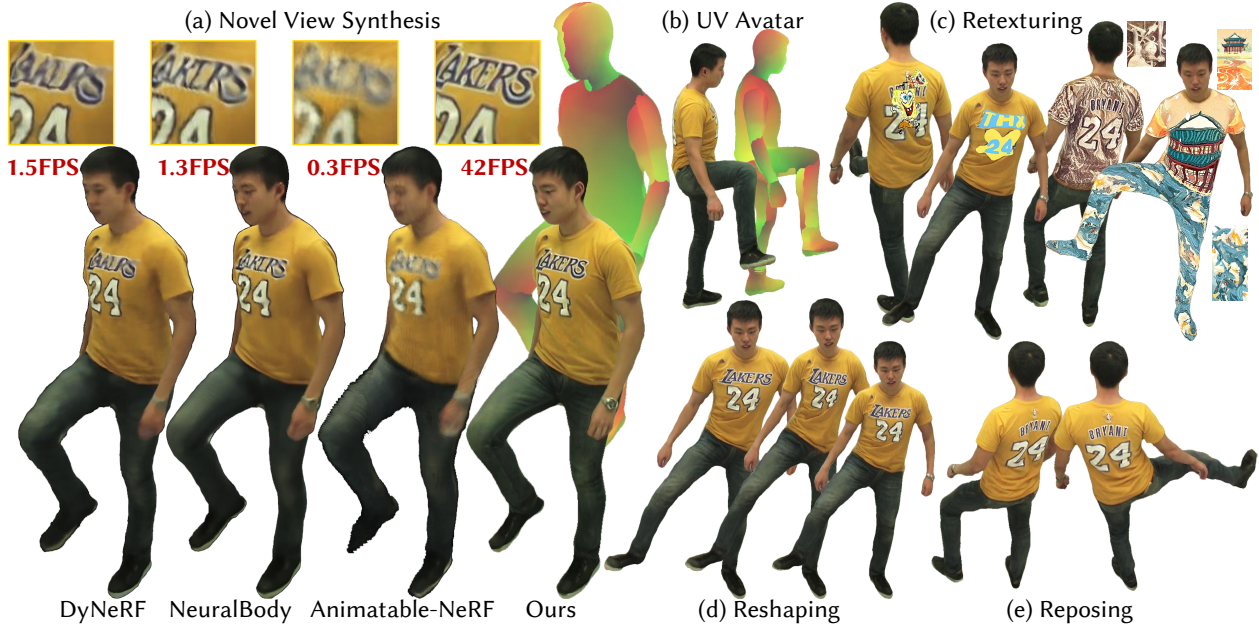


Figure 1. We decompose a dynamic human into 3D UV Volumes along with a 2D texture. The disentanglement of appearance and geometry enables us to achieve (a) high-fidelity real-time novel view synthesis guided by (b) a smooth UV avatar, (c) retexturing of a 3D human by editing a 2D texture, (d) reshaping and (e) reposing by changing the parameters of a human model while keeping the texture untouched.

Abstract

Neural volume rendering enables photo-realistic renderings of a human performer in free-view, a critical task in immersive VR/AR applications. But the practice is severely limited by high computational costs in the rendering process. To solve this problem, we propose the UV Volumes, a new approach that can render an editable free-view video of a human performer in real-time. It separates the high-frequency (i.e., non-smooth) human appearance from the 3D volume, and encodes them into 2D neural texture stacks (NTS). The smooth UV volumes allow much smaller and shallower neural networks to obtain densities and texture coordinates in 3D while capturing detailed appearance in 2D NTS. For editability, the mapping between the parameterized human model and the smooth texture coordinates allows us a better generalization on novel poses and shapes.

* Authors contributed equally to this work.

† Corresponding Author.

Furthermore, the use of NTS enables interesting applications, e.g., retexturing. Extensive experiments on CMU Panoptic, ZJU Mocap, and H36M datasets show that our model can render 960×540 images in 30FPS on average with comparable photo-realism to state-of-the-art methods. The project and supplementary materials are available at <https://fanegg.github.io/UV-Volumes>.

1. Introduction

Synthesizing a free-view video of a human performer in motion is a long-standing problem in computer vision. Early approaches [4] rely on obtaining an accurate 3D mesh sequence through multi-view stereo. However, the computed 3D mesh often fails to depict the complex geometry structure, resulting in limited photorealism. In recent years, methods (e.g., NeRF [35]) that make use of volumetric representation and differentiable ray casting have shown promising results for novel view synthesis. These tech-

niques have been further extended to tackle dynamic scenes.

Nonetheless, NeRF and its variants require a large number of queries against a deep Multi-Layer Perceptron (MLP). Such time-consuming computation prevents them from being applied to applications that require high rendering efficiency. In the case of static NeRF, a few methods [10, 44, 60] have already achieved real-time performance. However, for dynamic NeRF, solutions for real-time rendering of volumetric free-view video are still lacking.

In this work, we present *UV Volumes*, a novel framework that can produce an editable free-view video of a human performer in motion and render it in real-time. Specifically, we take advantage of a pre-defined UV-unwrapping (e.g., SMPL or dense pose) of the human body to tackle the geometry (with texture coordinates) and textures in two branches. We employ a sparse 3D Convolutional Neural Networks (CNN) to transform the voxelized and structured latent codes anchored with a posed SMPL model to a 3D feature volume, in which only smooth and view-independent densities and UV coordinates are encoded. For rendering efficiency, we use a shallow MLP to decode the density and integrate the feature into the image plane by volume rendering. Each feature in the image plane is then individually converted to the UV coordinates. Accordingly, we utilize the yielded UV coordinates to query the RGB value from a pose-dependent neural texture stack (NTS). This process greatly reduces the number of queries against MLPs and enables real-time rendering.

It is worth noting that the 3D Volumes in the proposed framework only need to approximate relatively “smooth” signals. As shown in Figure 2, the magnitude spectrum of the RGB image and the corresponding UV image indicates that UV is much smoother than RGB. That is, we only model the low-frequency density and UV coordinate in the 3D volumes, and then detail the appearance in the 2D NTS, which is also spatially aligned across different poses. The disentanglement also enhances the generalization ability of such modules and supports various editing operations.

We perform extensive experiments on three widely-used datasets: CMU Panoptic, ZJU Mocap, and H36M datasets. The results show that the proposed approach can effectively generate an editable free-view video from both dense and sparse views. The produced free-view video can be rendered in real-time with comparable photorealism to the state-of-the-art methods that have much higher computational costs. In summary, our major contributions are:

- A novel system for rendering editable human performance video in free-view and real-time.
- UV Volumes, a method that can accelerate the rendering process while preserving high-frequency details.
- Extended editing applications enabled by this framework, such as reposing, retexturing, and reshaping.

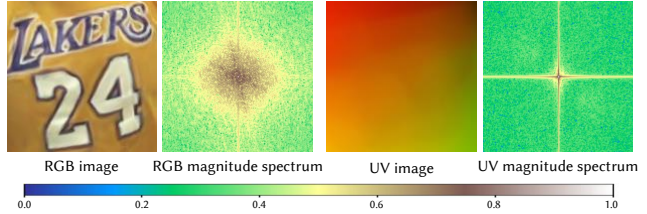


Figure 2. Discrete Fourier Transform (DFT) for RGB and UV image. In the magnitude spectrum, the distance from each point to the midpoint describes the frequency, the direction from each point to the midpoint describes the direction of the plane wave, and the value of the point describes its amplitude. The distribution of the UV magnitude spectrum is more concentrated in the center, which indicates that the frequency of the UV image is lower.

2. Related Work

Novel View Synthesis for Static Scenes. Novel view synthesis for static scenes is a well-explored problem. Early image-based rendering approaches [2, 6, 7, 14, 26] utilize densely sampled images to obtain novel views with light fields instead of explicit or accurate geometry estimation. The learning-based methods [8, 17, 24, 34, 49] apply neural networks to reuse input pixels from observed viewpoints. In recent years, dramatic improvements have been achieved by neural volume rendering techniques. For instance, NeRF [35] represents a static scene using a deep MLP, mapping 3D spatial locations and 2D viewing directions to volumetric density and radiance. For computation efficiency, rendering high-resolution scenes via NeRF is time-consuming since it requires millions of queries to obtain the density and radiance. Subsequent works [9, 10, 18, 37, 44, 60] attempt to accelerate the inference of vanilla NeRF in various ways, some of which achieve real-time rendering performance, but only for static scenes. For editability, the generative models, FENeRF [51] and IDE-3D [50], exploit semantic masks to edit the synthesized free-view portraits, but they are not compatible with the free-view performance capture task. NeuTex [58] also employs the UV-texture to store the appearance and enables editing on the texture map. Unfortunately, it can only tackle static objects.

Free-View Video Synthesis. Early methods [5, 36] rely on accurate 3D reconstruction and texture rendering captured by dome-based multi-camera systems to synthesize novel views of a dynamic scene. Recently, various neural representations have been employed in differentiable rendering to depict dynamic scenes, such as voxels [31], point clouds [57], textured meshes [1, 33, 52], and implicit functions [27, 29, 38, 39, 41, 42]. Particularly, DyNeRF [27] takes the latent code as the condition for time-varying scenes, while NeuralBody [41] employs structured latent codes anchored to a posed human model. Other deformation-based

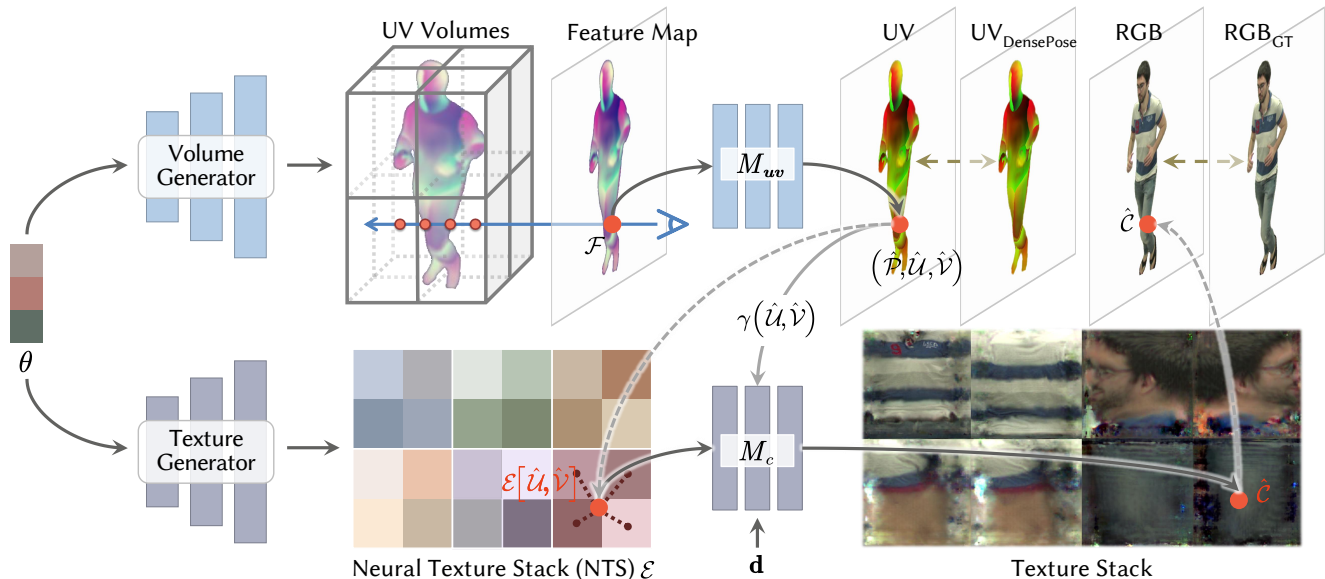


Figure 3. Overall pipeline of proposed framework. Our model has two main branches: 1) Based on a human pose θ , a volume generator constructs UV volumes involving the feature of UV information. Then a feature map can be rendered via differentiable raymarching and decoded to texture coordinates (UV) pixel-by-pixel. 2) A texture generator produces a pose-dependent Neural Texture Stack(NTS) \mathcal{E} that encodes the highly-detailed appearance information. The UV coordinates and the texture embedding interpolated from NTS are passed into an MLP to predict the color \hat{C} at the desired ray direction \mathbf{d} .

NeRF variants [28, 38, 39, 42, 53] take as input the monocular video, as a result, they fail to synthesize the free-view spatio-temporal visual effects. Besides, they also suffer from the high computational cost in inference and the lack of editing abilities. Geometric constraints and discrete space representation are exploited in methods [46, 61], and a hybrid scene representation is used for efficiency in [32, 45]. The method [55] employs Fourier PlenOctree to accelerate rendering, but the photorealism is harmed by the shared discrete representation across the time sequence. Furthermore, all these models are still non-editable.

Editable Free-View Videos. There exist previous works that focus on the problem of producing editable free-view videos or animatable avatars. ST-NeRF [62] exploits the layered neural representation in order to move, rotate and resize individual objects in free-view videos. Some methods [40, 56, 59] decompose a dynamic human into a canonical neural radiance field and a skeleton-driven warp field that backward maps observation-space points to canonical space. However, learning a backward warp field is highly under-constrained since the backward warp field is pose-dependent [3]. Textured Neural Avatars [47] proposes utilizing the texture map to improve novel pose generalization, whereas employing a 2D rendering neural network prevents it from consistent novel view synthesis. Neural Actor [30] takes the texture map as latent variables. Nevertheless, the requirement of the ground-truth texture map limits their application in many cases. In contrast, our approach esti-

mates the texture map end-to-end, and can produce editable (including reposing, reshaping and retexturing) free-view videos in real-time from both dense and sparse views.

3. Method

Given multi-view videos of a performer, our model generates an editable free-view video that supports real-time rendering. We use the availability of an off-the-shelf SMPL model and the pre-defined UV unwrap in Densepose [15] to introduce proper priors into our framework. In this section, we describe the details of our framework, which is shown in Figure 3. The two main branches in our framework are presented in turn. One is to generate the UV volumes (Sec. 3.1), and the other is the generation of NTS (Sec. 3.2). Then we provide a more detailed description of the training process in Sec. 3.3.

3.1. UV Volumes

Neural radiance fields [35] have been proven to produce free-viewpoint images with view consistency and high fidelity. Nonetheless, capturing the high-fidelity appearance in a dynamic scene is time-consuming and difficult. To this end, we propose the UV volumes in which only the density and texture coordinate (i.e., UV coordinate) are encoded instead of human appearance. Given the UV image rendered by ray casting, we can use the UV coordinates to query the corresponding RGB values from the 2D NTS by employing the UV unwrap defined in Densepose.

We utilize the volume generator to construct UV volumes. First, the time-invariant latent codes anchored to a posed SMPL model are voxelized and taken as the input. Then we use the 3D sparse CNN to encode the voxelized latent codes to a 3D feature volume named UV volumes, which contains UV information.

Given a sample image \mathcal{I} of multi-view videos, we provide a posed SMPL parameterized by human pose θ and a set of latent codes \mathbf{z} anchored on its vertices and then query the feature vector $f(\mathbf{x}, \mathbf{z}, \theta)$ at point \mathbf{x} from the generated UV volumes. The feature vector is fed into a shallow MLP M_σ to predict the volume density:

$$\sigma(\mathbf{x}) = M_\sigma(f(\mathbf{x}, \mathbf{z}, \theta)). \quad (1)$$

We then apply the volume rendering [23] technique to render the UV feature volume into a 2D feature map. We sample N_i points $\{\mathbf{x}_i\}_{i=1}^{N_i}$ along the camera ray \mathbf{r} between near and far bounds based on the posed SMPL model in 3D space. The feature at the pixel can be calculated as:

$$\mathcal{F}(\mathbf{r}) = \sum_{i=1}^{N_i} T_i (1 - \exp(-\sigma(\mathbf{x}_i) \delta_i)) f(\mathbf{x}_i, \mathbf{z}, \theta), \quad (2)$$

$$\text{where } T_i = \exp\left(-\sum_{j=1}^{i-1} \sigma(\mathbf{x}_j) \delta_j\right),$$

and $\delta_i = \|\mathbf{x}_{i+1} - \mathbf{x}_i\|_2$ is the distance between adjacent sampled points. An MLP M_{uv} is then used to individually decode all the pixels in the yielded view-invariant feature map to their corresponding texture coordinates and generate the UV image. In specific, the texture coordinates can be represented as:

$$\left(\hat{\mathcal{P}}(\mathbf{r}), \hat{\mathcal{U}}(\mathbf{r}), \hat{\mathcal{V}}(\mathbf{r})\right) = M_{uv}(\mathcal{F}(\mathbf{r})), \quad (3)$$

where $\hat{\mathcal{P}}$ and $\hat{\mathcal{U}}, \hat{\mathcal{V}}$ are the corresponding part assignments and UV coordinates, respectively.

3.2. Neural Texture Stack

Given the generated UV image, we employ the continuous texture stack encoded in the implicit neural representation to recover the color image. To extract the local relation of the neural texture stack with respect to the human pose, we use a CNN texture generator G to produce the pose-dependent NTS:

$$\mathcal{E}_k = G(\theta, \mathbf{k}), \quad (4)$$

where we subdivide the body surface into $N_k = 24$ parts, and \mathbf{k} is a one-hot label vector representing the k -th body part. At a foreground pixel, the part assignments $\hat{\mathcal{P}}$ predicted from UV volumes (referred in Equation (3)) can be interpreted as the probability of the pixel belonging to the k -th body part, which is defined as $\sum_{k=1}^{N_k} \hat{\mathcal{P}}_k(\mathbf{r}) = 1$. For

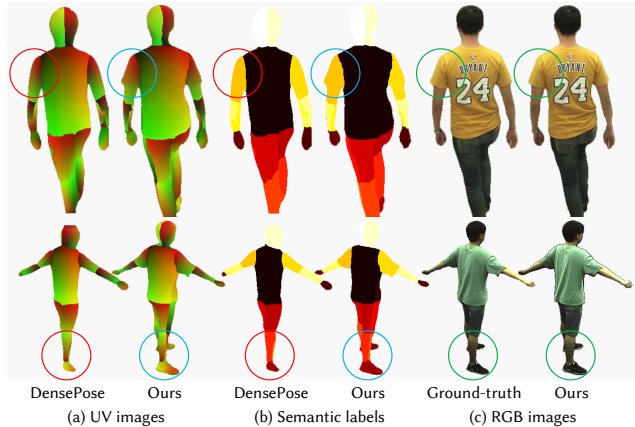


Figure 4. Given noisy UV and semantic labels (e.g., red circles), we can recover proper UV volumes (e.g., blue circles) under the intrinsic multi-view constraint of minimizing the photometric error between renderings and ground-truth (e.g., green circles).

each human body part k , the texture generator generates the corresponding neural texture stack \mathcal{E}_k . We forward propagate the generator network G once to predict the neural textures with a batch size of 24. Let $\hat{\mathcal{U}}_k$ and $\hat{\mathcal{V}}_k$ denote the predicted UV coordinates of the k -th body part. We sample the texture embeddings at non-integer locations ($\hat{\mathcal{U}}_k(\mathbf{r}), \hat{\mathcal{V}}_k(\mathbf{r})$) in a piecewise-differentiable manner using bilinear interpolation [20]:

$$\mathbf{e}_k(\mathbf{r}) = \mathcal{E}_k\left[\hat{\mathcal{U}}_k(\mathbf{r}), \hat{\mathcal{V}}_k(\mathbf{r})\right]. \quad (5)$$

To model the high-frequency color of human performances, we apply positional encoding $\gamma(\cdot)$ [43] to UV coordinates and the viewing direction, and pass the encoded UV map along with the sampled texture embedding into an MLP M_c to decode the view-dependent color $\hat{\mathcal{C}}_k(\mathbf{r})$ of camera ray \mathbf{r} at the desired viewing direction \mathbf{d} :

$$\hat{\mathcal{C}}_k(\mathbf{r}) = M_c\left(\gamma(\hat{\mathcal{U}}_k(\mathbf{r}), \hat{\mathcal{V}}_k(\mathbf{r})), \mathbf{e}_k(\mathbf{r}), \mathbf{k}, \gamma(\mathbf{d})\right). \quad (6)$$

Following that, the color $\hat{\mathcal{C}}(\mathbf{r})$ at each pixel is reconstructed via a weighted combination of decoded colors at N_k body parts, where the weights are prescribed by part assignments $\hat{\mathcal{P}}_k$:

$$\hat{\mathcal{C}}(\mathbf{r}) = \sum_{k=1}^{N_k} \hat{\mathcal{P}}_k(\mathbf{r}) \hat{\mathcal{C}}_k(\mathbf{r}). \quad (7)$$

3.3. Training

Collecting the results of all rays $\{\hat{\mathcal{C}}(\mathbf{r})\}^{H \times W}$, we denote the entire rendered image as $\hat{\mathcal{I}} \in \mathbb{R}^{H \times W \times 3}$. To learn the parameters of our model, we optimize the photometric error



Figure 5. The novel view synthesis of our model on various human performances, which achieves high-fidelity renderings in real-time.

between the renderings $\hat{\mathcal{I}}$ and the ground-truth images \mathcal{I} :

$$\mathcal{L}_{\text{rgb}} = \left\| \hat{\mathcal{I}} - \mathcal{I} \right\|_2^2. \quad (8)$$

Benefiting from our memory-saving framework that disentangles appearance and geometry, we can render an entire image during training instead of sampling image patches [35, 41]. Thus, we also compare the rendered images against the ground-truth using perceptual loss [11, 21, 54], which extracts feature maps by a pretrained fixed VGG network $\psi(\cdot)$ [48] from both images and minimizes the L1-norm between them:

$$\mathcal{L}_{\text{vgg}} = \left\| \psi(\hat{\mathcal{I}}) - \psi(\mathcal{I}) \right\|_1. \quad (9)$$

To warm-start the UV volumes and regularize its solution space, we leverage the pre-trained DensePose model as an auxiliary supervisor. In particular, we perform the DensePose network on the training data and utilize the outputs of DensePose as pseudo supervision, such that we can regularize UV volumes by semantic loss \mathcal{L}_p and UV-metric loss \mathcal{L}_{uv} between DensePose outputs and our UV images:

$$\begin{aligned} \mathcal{L}_p &= \sum_{k=1}^{N_k} \mathcal{P}_k \log(\hat{\mathcal{P}}_k), \\ \mathcal{L}_{\text{uv}} &= \sum_{k=1}^{N_k} \mathcal{P}_k \left(\left\| \hat{\mathcal{U}}_k - \mathcal{U}_k \right\|_2^2 + \left\| \hat{\mathcal{V}}_k - \mathcal{V}_k \right\|_2^2 \right), \end{aligned} \quad (10)$$

where N_k is the number of body parts, and \mathcal{P}_k and $\hat{\mathcal{P}}_k$ are respectively the multi-class semantic probability at the k -th part of DensePose outputs and UV images. Similarly, $\mathcal{U}_k, \mathcal{V}_k$ and $\hat{\mathcal{U}}_k, \hat{\mathcal{V}}_k$ are the predicted UV coordinates at the k -th part of DensePose and UV images, respectively. \mathcal{L}_p is chosen as a multi-class cross-entropy loss to encourage rendered part labels to be consistent with provided DensePose labels, and \mathcal{L}_{uv} promotes to generate inter-frame consistent UV coordinates.

We present the UV images predicted by our UV volumes and the pseudo supervision of DensePose in Figure 4. Given noisy semantic and UV labels (e.g., the red circles), we can reconstruct proper UV volumes (e.g., the blue circles) under the intrinsic multi-view constraint of RGB loss (e.g., the green circles). As shown in the second row of Figure 4, it can be observed that UV volumes successfully recover the UV images even though the provided DensePose supervision is incorrect.

Given the binary human mask \mathcal{S} for the observed image \mathcal{I} , we propose a silhouette loss to facilitate UV volumes modeling a more fine-grained geometry:

$$T(\mathbf{r}) = \exp \left(- \sum_{j=1}^{N_i-1} \sigma(\mathbf{x}_j) \delta_j \right), \quad (11)$$

$$\mathcal{L}_s = \sum_{\mathbf{r} \in \mathcal{R}} (\mathcal{S}(\mathbf{r})(1 - T(\mathbf{r})) + (1 - \mathcal{S}(\mathbf{r}))T(\mathbf{r})),$$

where $T(\mathbf{r})$ is accumulated transmittance. Here we define the value of mask $\mathcal{S}(\mathbf{r})$ in the foreground as zero, and the background as one.

We combine the aforementioned losses and jointly train our model to optimize the full objective:

$$\mathcal{L} = \mathcal{L}_{\text{rgb}} + \lambda_{\text{vgg}} \mathcal{L}_{\text{vgg}} + \lambda_p \mathcal{L}_p + \lambda_{\text{uv}} \mathcal{L}_{\text{uv}} + \lambda_s \mathcal{L}_s. \quad (12)$$

4. Experiments

To demonstrate the effectiveness and efficiency of our method, we perform extensive experiments. We report quantitative results using four standard metrics: PSNR, SSIM, LPIPS, and FPS¹. And the qualitative experiments further illustrate that our method produces photo-realistic images in different tasks, e.g., novel view synthesis, reposing, reshaping, and retexturing.

¹The sparse CNN output is pre-computed for the reported framerates.

| Datasets | | View synthesis quality | | | | | | | | | | | | | | Efficiency | | | | |
|-------------------|------|------------------------|--------------|-------|---------------------|--------------|-----------------|--------------|--------------|---------------------|--------------|--------------------|-------|-------|---------------------|----------------|------|------|------|--------------|
| | | PSNR \uparrow | | | | | SSIM \uparrow | | | | | LPIPS \downarrow | | | | FPS \uparrow | | | | |
| | | DN | NB | AN | w/o \mathcal{L}_p | Ours | DN | NB | AN | w/o \mathcal{L}_p | Ours | DN | NB | AN | w/o \mathcal{L}_p | Ours | DN | NB | AN | Ours |
| CMU (960×540) | p1 | 30.04 | 29.78 | 27.12 | 30.09 | 30.38 | 0.968 | 0.962 | 0.936 | 0.963 | 0.966 | 0.088 | 0.099 | 0.135 | 0.055 | 0.036 | 1.01 | 0.76 | 0.21 | 44.76 |
| | p2 | 25.56 | 25.68 | 26.13 | 28.51 | 28.78 | 0.939 | 0.942 | 0.903 | 0.952 | 0.953 | 0.137 | 0.139 | 0.204 | 0.062 | 0.044 | 1.45 | 1.28 | 0.34 | 37.30 |
| | p3 | 27.04 | 27.12 | 24.20 | 29.36 | 29.38 | 0.955 | 0.956 | 0.874 | 0.962 | 0.962 | 0.154 | 0.142 | 0.259 | 0.062 | 0.047 | 2.12 | 1.28 | 0.33 | 34.60 |
| ZJU (512×512) | 313 | 29.67 | 28.82 | 27.50 | 28.44 | 29.11 | 0.958 | 0.952 | 0.939 | 0.956 | 0.958 | 0.084 | 0.088 | 0.124 | 0.068 | 0.053 | 2.07 | 1.51 | 0.62 | 51.39 |
| | 377 | 27.13 | 28.12 | 25.71 | 26.18 | 26.28 | 0.933 | 0.949 | 0.923 | 0.931 | 0.930 | 0.112 | 0.088 | 0.152 | 0.094 | 0.085 | 2.41 | 2.02 | 0.76 | 38.70 |
| | 386 | 30.29 | 30.12 | 28.51 | 28.38 | 28.48 | 0.938 | 0.939 | 0.915 | 0.919 | 0.916 | 0.122 | 0.112 | 0.163 | 0.103 | 0.078 | 3.00 | 4.89 | 0.91 | 35.88 |
| H36M (500×500) | s9p | 21.53 | 25.11 | 26.08 | 26.03 | 26.19 | 0.824 | 0.912 | 0.917 | 0.915 | 0.916 | 0.242 | 0.136 | 0.139 | 0.085 | 0.084 | 1.06 | 2.19 | 0.30 | 40.00 |
| | s11p | 21.27 | 24.39 | 25.21 | 25.20 | 25.82 | 0.828 | 0.899 | 0.906 | 0.905 | 0.911 | 0.313 | 0.193 | 0.174 | 0.118 | 0.111 | 1.18 | 1.02 | 0.67 | 33.41 |
| | s1p | 18.91 | 23.24 | 23.43 | 23.83 | 23.98 | 0.781 | 0.909 | 0.901 | 0.911 | 0.911 | 0.332 | 0.149 | 0.162 | 0.094 | 0.093 | 1.38 | 0.97 | 0.50 | 41.43 |

Table 1. Quantitative results of **novel view synthesis**. We present competitive PSNR and SSIM while outperforming baselines on LPIPS (agrees well with human visual perception [63]) and achieve 30 FPS (pre-computed sparse CNN) available for real-time applications.

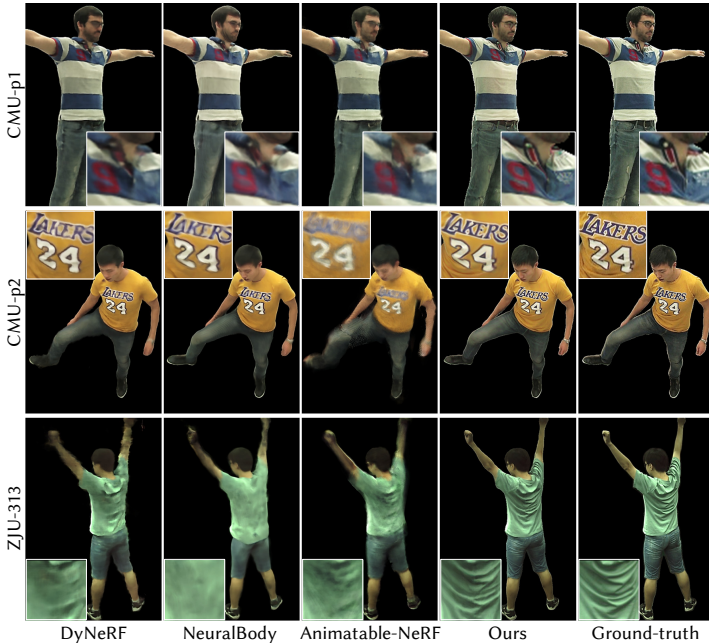


Figure 6. Qualitative results of **novel view synthesis** on CMU Panoptic and ZJU Mocap. Benefiting from spatially aligning the appearance across different poses in a 2D texture, our method produces high-fidelity novel view synthesis, while baselines suffer from blurs (at letters and wrinkles).

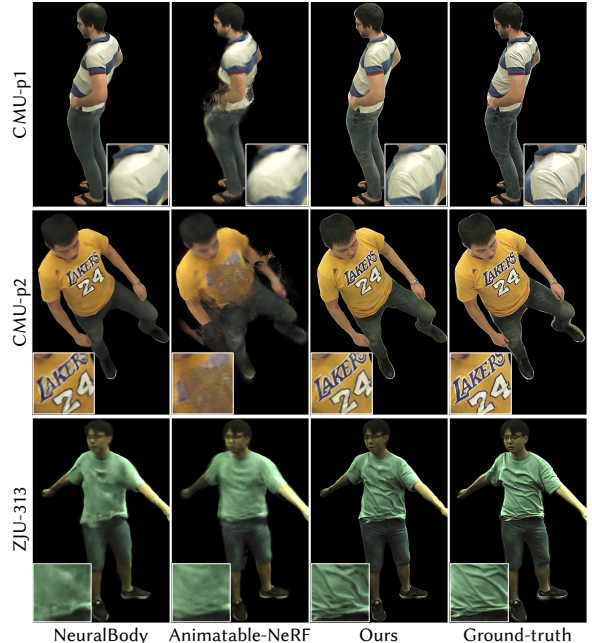


Figure 7. Qualitative results of **novel pose synthesis** on CMU Panoptic, ZJU Mocap. Benefiting from the disentanglement of appearance and geometry, our method performs better on novel poses, especially for preserving sharp details.

Dataset. We perform experiments on several types of datasets which consist of calibrated and synchronized multi-view videos. We use 26 and 20 training views on CMU Panoptic dataset [22] with 960×540 resolution and ZJU Mocap dataset [41] with 512×512 resolution, respectively. The most challenging one is the H36M dataset [19] with 500×500 resolution, where only three cameras are available for training. We obtain the binary human mask by [13]. The evaluation is done on the hold-out cameras (novel views) or hold-out segments of the sequence (novel poses).

Baselines. To validate our method, we compare it against several state-of-the-art free-view video synthesis techniques: 1) DN: DyNeRF [27], which takes time-varying

latent codes as the conditions for dynamic scenes; and 2) NB: NeuralBody [41], which takes as input the posed human model with structured time-invariant latent codes and generates a pose-conditioned neural radiance field; 3) AN: Animatable-NeRF [40], which uses neural blend weight fields to generate correspondences between observation and canonical space.

Novel View Synthesis. For comparison, we synthesize images of training poses in hold-out test views. Table 1 shows the comparison of our method against baselines, which demonstrates that our method performs best LPIPS and FPS among all methods. Specifically, we achieve rendering free-view videos of human performances in 30FPS with the help

| Method | CMU (960×540) | | | ZJU (512×512) | | | H36M (500×500) | | |
|--------|---------------|--------|---------|---------------|--------|---------|----------------|--------|---------|
| | PSNR ↑ | SSIM ↑ | LPIPS ↓ | PSNR ↑ | SSIM ↑ | LPIPS ↓ | PSNR ↑ | SSIM ↑ | LPIPS ↓ |
| NB | 25.94 | 0.918 | 0.146 | 24.51 | 0.918 | 0.120 | 25.54 | 0.884 | 0.170 |
| AN | 23.65 | 0.883 | 0.208 | 24.55 | 0.911 | 0.153 | 25.00 | 0.873 | 0.170 |
| Ours | 26.20 | 0.927 | 0.073 | 23.69 | 0.910 | 0.104 | 25.04 | 0.874 | 0.141 |

Table 2. Quantitative results of **novel pose synthesis**. We achieve competitive PSNR and SSIM while outperforming baselines on LPIPS, which agrees well with humans [63].

of UV volumes. Note that LPIPS agrees surprisingly well with human visual perception [63], which indicates that our synthesis is more visually similar to ground-truth.

Figure 6 presents the qualitative comparison of our method with baselines. Baselines fail to preserve the sharp image details, whose rendering is blurry and even split. In contrast, our method can accurately capture high-frequency details like letters, numbers and wrinkles on shirts and the belt on pants benefiting from our NTS model. Furthermore, we show the view synthesis results of dynamic humans in Figure 5, which indicate that our method generates high-quality appearance results even with rich textures and challenging motions. Note that the rightmost example is from the H36M dataset with only 4 views. Please refer to the supplementary material for more results.

Reposing. We perform reposing on the human performer with novel motions. As DyNeRF is not designed for editing tasks, we compare our method against NeuralBody and Animatable-NeRF. As shown in Table 2, quantitative results demonstrate that our method achieves competitive PSNR and SSIM while outperforming others on LPIPS.

The qualitative results are shown in Figure 7. For novel human poses, NeuralBody gives blurry and distorted rendering results, while Animatable-NeRF even produces split humans due to a highly under-constrained backward warp field from observation to canonical space. In contrast, synthesized images of our method exhibit better visual quality with reasonable high-definition dynamic textures. The results indicate that using smooth UV volumes in 3D and encoding texture in 2D has better controllability on the novel pose generalization than directly modeling a pose-conditioned neural radiance field.

Reshaping. We demonstrate that our approach can edit the shape of reconstructed human performance by changing the shape parameters of the SMPL model. We illustrate the qualitative results in Figure 1 and Figure 8. NeuralBody fails to infer the reasonable changes of the cloth, while our method generalizes well on novel shapes.

Retexturing. With the learned dense correspondence of UV volumes and neural texture, we can edit the 3D cloth with a user-provided 2D texture, as shown in Figure 9. Visually inspected, the rich texture patterns are well preserved and transferred to correct semantic areas in different poses. Moreover, our model supports changing textures’ style and appearance, which are presented in Figure 10. Thanks to

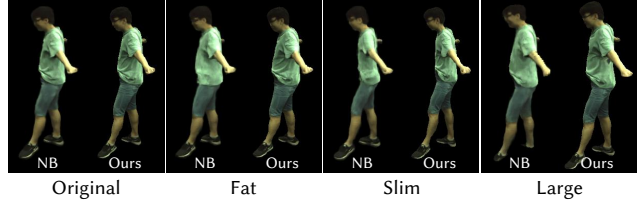


Figure 8. Qualitative results of **reshaping**. By changing the SMPL parameters β , we can conveniently make the human performer fatter, slimmer, or larger. The result of NeuralBody is shown on the left of each image pair, while ours is on the right. Obviously, more details and consistency are preserved by ours in varying shapes.



Figure 9. Qualitative results of **retexturing**. The disentanglement of appearance and geometry allows us to conveniently edit the texture by drawing patterns on the NTS. The rich texture patterns are well preserved and transferred to correct semantic areas in different poses, which demonstrates that the texture is not only changed as expected under the edited frame, but also transferred to a novel frame with the modeled dynamics.

the style transfer network [12], we can perform arbitrary artistic stylizations on 3D human performance. Given any fabric texture, we can even dress the performer in various appearances, which enables 3D virtual try-on in real-time.

4.1. Ablation Studies

We conduct ablation studies on performer p1 of the CMU dataset. As shown in Table 3, we analyze the effects of different losses for the proposed approach by removing warm-start loss, perceptual loss and silhouette loss, respectively. Then, we analyze the time consumption of each module. We encourage the reader to see the supplement for additional ablations, discussion of model design, and other experimental results.

Impact of warm-start loss. We present using semantic and UV-metric loss to warm-start the UV volumes and constrain its solution space. To prove the effectiveness of this process, we train an ablation (No Warm-start Loss) built upon our full model by eliminating the warm-start loss. It gives a lower performance in all metrics, especially the LPIPS in-



Figure 10. Given any arbitrary artistic style or cloth appearance, we can render (a) a 3D dynamic human with the transferred texture or perform (b) a 3D virtual try-on in real-time.

| Ablations | Novel View Synthesis | | | Novel Pose Generation | | |
|--------------------|----------------------|-----------------|--------------------|-----------------------|-----------------|--------------------|
| | PSNR \uparrow | SSIM \uparrow | LPIPS \downarrow | PSNR \uparrow | SSIM \uparrow | LPIPS \downarrow |
| No Warm-start Loss | 30.37 | 0.964 | 0.060 | 26.14 | 0.917 | 0.076 |
| No Perceptual Loss | 30.09 | 0.963 | 0.055 | 26.05 | 0.919 | 0.079 |
| No Silhouette Loss | 17.47 | 0.874 | 0.207 | 16.95 | 0.860 | 0.218 |
| Complete Model | 30.38 | 0.966 | 0.036 | 26.20 | 0.927 | 0.073 |

Table 3. Ablation study about different objective functions.

creased a lot when rendering novel views. This comparison indicates that the warm-start loss yields better information reuse of different frames by transforming the observation XYZ coordinates to canonical UV coordinates defined by the consistent semantic and UV-metric loss.

Impact of perceptual loss. In contrast to sampling image patches as baselines, we can render an entire image during training, allowing us to use perceptual loss. Table 3 shows that using the same model but training without the perceptual loss (No Perceptual Loss) gives a lower performance in all metrics, especially the PSNR and LPIPS. It demonstrates that the perceptual loss is of critical importance to improving the visual quality of synthesized images, which is also reflected in Table 1 (w/o \mathcal{L}_p).

Impact of silhouette loss. To facilitate the UV volumes modeling a more fine-grained geometry, we employ a silhouette loss by using the 2D binary mask of the human performer. We present an ablation (No Silhouette Loss) built upon our full model by eliminating the silhouette loss, as shown in Table 3. It is obvious that No Silhouette Loss gives the worst performance in all metrics among all ablations. This comparison shows that our geometry does benefit from the silhouette loss, which can be seen in the supplement to get an intuitive visual impression.

4.2. Time Consumption

We analyze the time consumption of each module in our framework and the corresponding module in Neural-

| Method | Novel Pose Generation | | | | | |
|--------|-----------------------|----------------------|-------------|------|-----------|------|
| | Sparse CNN | Novel View Synthesis | | | Rendering | |
| | | Density | Color Model | | | |
| Ours | 48.78 | 7.08 | UV | NTS | RGB | 1.73 |
| | | | 1.53 | 7.52 | 1.60 | |
| | | | 9.12 | | | |
| | | | 19.46 | | | |
| 68.23 | | | | | | |
| NB | 52.04 | 84.38 | 546.81 | | 32.65 | |
| | | 663.84 | | | | |
| | | 715.88 | | | | |

Table 4. Time consumption of each module in milliseconds(ms).

Body [41] on ZJU Mocap performer 313, as shown in Table 4. On average, it takes 48.78 ms for us to obtain the UV volumes from the posed human model. Then, our method takes only 19.46 ms (51FPS) to access the free-view renderings, which benefits from the smooth UV volumes that allow using much smaller and shallower MLP to obtain densities and texture coordinates in 3D while capturing detailed appearance in 2D NTS. On the contrary, NeuralBody spends 663.84 ms (1.5FPS) to synthesize novel views, which prevents it from being used in applications that require running in real-time. Even on the novel pose generalization task, our method can reach 68.23 ms per frame (14FPS) as well. All experiments are run on a single NVIDIA A100 GPU.

4.3. Limitation

Our method leverages the SMPL model as a scaffold and DensePose as supervision. Consequently, our method can handle clothing types that roughly fit the human body, but fails to correct the prediction from DensePose when handling long hair, loose clothing, accessories, and photorealistic hands. Therefore, the future work is to utilize explicit cloth models and extra hand tracking. While we use time-invariant structured latent codes to encourage temporally consistent UV, a little perturbation caused by the volume generator may occur in the dynamic human (e.g., some unnatural sliding on the trouser when retexturing the performer). It might be improved by adding temporal consistency loss. Replacing the volume representation with other sparse structures for efficiency is also promising.

5. Conclusions

We present the UV volumes for free-view video synthesis of a human performer. It is the first method to generate a real-time free-view video with editing ability. The key is to employ the smooth UV volumes and highly-detailed textures in an implicit neural texture stack. Extensive experiments demonstrate both the effectiveness and efficiency of our method. In addition to improving efficiency, our approach can also support editing, e.g., reposing, reshaping, or retexturing the human performer in the free-view videos.

Here we provide more implementation details and experimental results. We encourage the reader to view the video results included in the supplementary materials for an intuitive experience of editable free-view human performance.

A. Network Architectures

A.1. Volume Generator

We utilize the volume generator to construct UV volumes, which is presented in Figure 11. We take the human pose as input to the SMPL model and animate human point clouds in different poses. Then we follow the previous work [41] to anchor a set of time-invariant latent codes to the posed human point cloud and voxelize the point cloud. We follow the network architecture of [41] to model the 3D sparse CNN, and reduce the channels from 352 to 64, since the UV volumes only capture low-frequency semantic information.

A.2. Density, IUUV and Color Network

We present architectures of density network M_σ , IUUV network M_{uv} and color network M_c in Figure 12, Figure 13 and Figure 14, respectively.

A.3. Texture Generator

Figure 15 shows the architecture of convolutional texture generator network G . For each human body part of $\{i\}_{i=1}^{24}$, the texture generator generates a corresponding neural texture stack of $\{\mathcal{E}_i\}_{i=1}^{24}$. To predict the specific pose-dependent \mathcal{E}_i , we concatenate human pose vector θ with a one-hot body part label vector \mathbf{k}_i as input to the texture generator. We forward propagate the generator network G once to predict all the 24 textures with a batch size of 24. The CNN-based module is developed to extract the local relation of neural texture stack with respect to the human pose. The output spatial neural texture stacks (NTS) will be used for UV unwrapping subsequently.

B. Additional Implementation Details

We set λ_{vgg} to 5×10^{-2} and λ_s to 1×10^{-1} . The λ_p and λ_{uv} are exponential annealing from 1×10^{-1} and 1×10^{-0} to 1×10^{-3} and 5×10^{-2} with $k = 4 \times 10^{-2}$:

$$\begin{aligned} \lambda_p &= \max(1 \times 10^{-1} e^{-k \cdot \text{epoch}}, 1 \times 10^{-3}) \\ \lambda_{\text{uv}} &= \max(1 \times 10^{-0} e^{-k \cdot \text{epoch}}, 5 \times 10^{-2}) \end{aligned} \quad (13)$$

As shown in Figure 16a, the weight of UV-metric is large at the beginning because UV volumes require a warm-start to satisfy the UV unwrap defined by DensePose [16], and then drop rapidly within 100 epochs because DensePose outputs are not accurate. After 100 epochs, UV-metric becomes a regular term used to constrain the solution space of UV volumes.

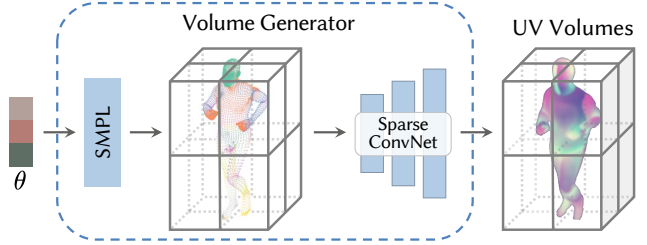


Figure 11. Architecture of the volume generator. It takes human pose θ as input, drives the point clouds parameterized by the SMPL model under the control of θ , and generates the UV volumes using a 3D sparse CNN to encode a set of latent codes \mathbf{z} anchored on the posed point clouds.

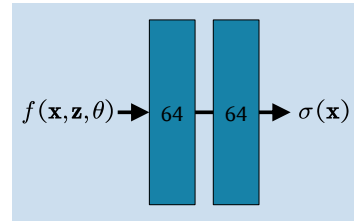


Figure 12. Architecture of the density network. The network takes the feature vector $f(\mathbf{x}, \mathbf{z}, \theta)$ at point \mathbf{x} interpolated by the generated UV volumes and outputs density $\sigma(\mathbf{x})$ using ReLU activation. The shallow density MLP M_σ consists of 2 fully-connected layers with 64 channels.

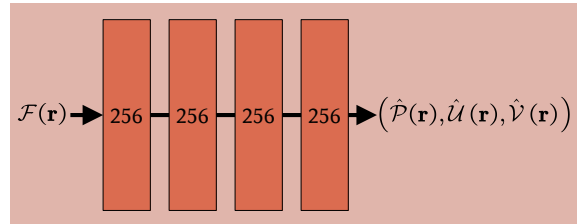


Figure 13. Architecture of the IUUV network. The network takes the rendered UV feature vector $\mathcal{F}(\mathbf{r})$ at camera ray \mathbf{r} and outputs view-invariant texture coordinates $(\hat{P}(\mathbf{r}), \hat{U}(\mathbf{r}), \hat{V}(\mathbf{r}))$ using sigmoid activation. The IUUV MLP M_{uv} is modeled by 4 fully-connected layers of 256 channels.

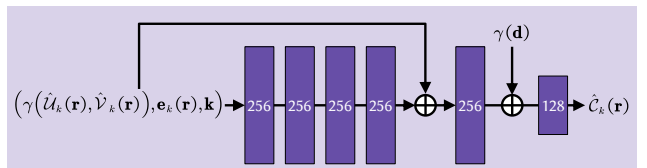


Figure 14. Architecture of the color network. The network takes positional encoding of texture coordinates $\gamma(\hat{U}_k(\mathbf{r}), \hat{V}_k(\mathbf{r}))$ along with the sampled texture embeddings at locations $(\hat{U}_k(\mathbf{r}), \hat{V}_k(\mathbf{r}))$ and a one-hot part label vector \mathbf{k} . The color MLP M_c is modeled by 5 fully-connected layers of 256 channels, including a skip connection that concatenates inputs to the fourth layer's activation. The feature vector of the fifth layer is processed by an additional layer with 128 channels, along with positional encoding of input viewing direction $\gamma(\mathbf{d})$. A final layer with a sigmoid activation outputs view-dependent RGB color $\hat{C}_k(\mathbf{r})$ of body part \mathbf{k} .

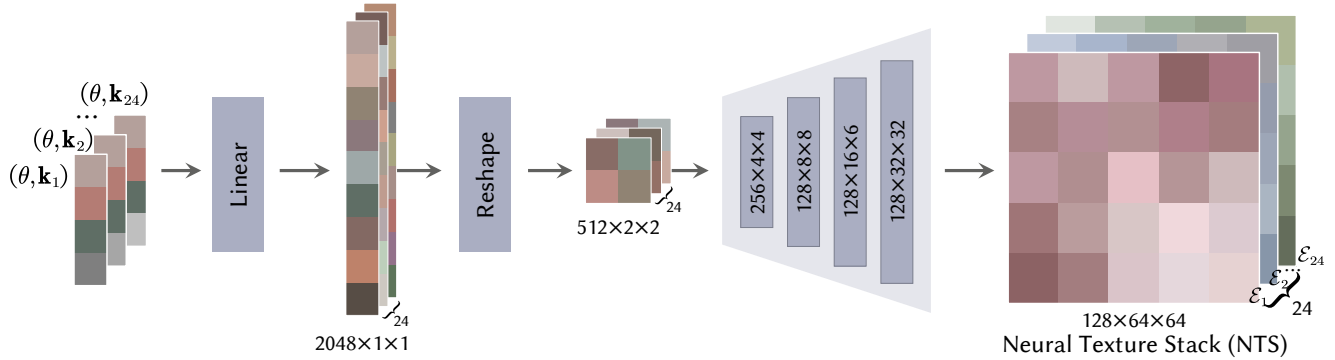


Figure 15. Convolutional texture generator network G consists of 5 convolution layers to get the neural texture stack \mathcal{E}_i with 128 dimensions.

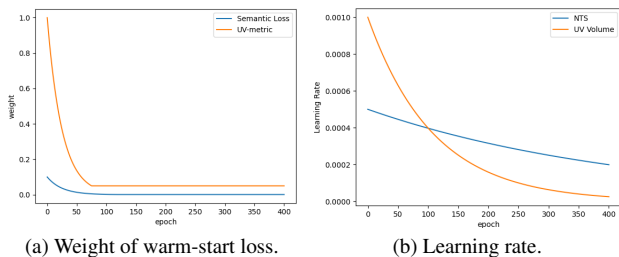


Figure 16. (a) The blue represents the weight of semantic loss λ_p and the orange represents the weight of UV-metric loss \mathcal{L}_{uv} . (b) The orange represents the learning rate of the UV volumes branch and the blue represents the learning rate of the NTS branch.

UV volumes should be learned primarily in the early stages of training, because The NTS makes sense only after the UV volumes warm-start and a coarse geometry is constructed. Conversely, later in training, we optimize NTS to fit high-frequency signals rather than UV coordinates. Therefore, we use two optimization strategies to train the UV volumes and NTS branch. Their learning rates start from 1×10^{-3} and 5×10^{-4} with a decay rate of $\gamma = 1 \times 10^{-1}$, respectively, and decay exponentially along the optimization, as shown in Figure 16b.

$$\begin{aligned} l_{nts} &= 5 \times 10^{-4} \gamma^{\frac{\text{epoch}}{1000}} \\ l_{uv} &= 1 \times 10^{-3} \gamma^{\frac{\text{epoch}}{250}} \end{aligned} \quad (14)$$

In our experiments, we sample camera rays all over an entire image and 64 points along each ray between near and far bounds. The scene bounds are estimated based on the SMPL model. We adopt the Adam optimizer [25] for training our model. We conduct the training on a single NVIDIA A100 GPU. The training on 26-view videos of 100 frames at 960×540 resolution typically takes around 200k iterations to converge (about 20 hours).

C. Additional Baseline Method Details

DyNeRF (DN) [27]. We reimplement DN by following the procedure in their paper to train the model on video sequences of a moving human.

Neural Body (NB) [41]. We use the NB code open-sourced by the authors at <https://github.com/zju3dv/neuralbody> and follow their procedure for training on video sequences of a moving human.

Animatable NeRF (AN) [40]. We use the AN code open-sourced by the authors at <https://github.com/zju3dv/animatable> and follow their procedure for training on video sequences of a moving human.

D. Additional Ablation Studies

We conduct ablation studies on performer p1 of the CMU dataset. As shown in Table 5, Table 6, Table 7, Figure 20, Figure 21, and Figure 22, we analyze the effects of different losses for our proposed approach, different types of NTS, different resolutions of NTS, different methods to model the view-dependent color, and different experimental settings of video frames and input views.

D.1. Effects of Different Losses

Impact of warm-start loss. No Warm-start Loss (w/o \mathcal{L}_{uv}) is an ablation built upon our full model by eliminating the warm-start loss. As shown in Figure 20 and Figure 21, w/o \mathcal{L}_{uv} suffers from ambiguity, like the belt on the pants and meaningless texture. This comparison indicates that the warm-start loss yields better information reuse of different frames by transforming the observation XYZ coordinates to canonical UV coordinates defined by the consistent semantic and UV-metric loss.

Impact of perceptual loss. No Perceptual Loss (w/o \mathcal{L}_{vgg}) is an ablation that uses the same model but training without the perceptual loss. As shown in Figure 20 and Figure 21, w/o \mathcal{L}_{vgg} suffers from blur, like the number 9 on the shirt

and distorted number 9 on the texture. This comparison illustrates that perceptual loss can improve the visual quality of synthesized images by supervising the structure of the renderings from local to global during training.

Impact of silhouette loss. No Silhouette Loss (w/o \mathcal{L}_s) is an ablation built upon our full model by eliminating the silhouette loss. As shown in Figure 20, w/o \mathcal{L}_s suffers from artifacts around the performance because there is no the warm-start supervision of semantic and UV-metric labels around the boundary. This comparison demonstrates that silhouette loss is essential for us to model fine-grained geometry.

D.2. Neural Texture Stacks

We performed two ablations: 1) different types of NTS; 2) NTS at different resolutions to illuminate the design decisions for the proposed *Neural Texture Stacks*.

Different Types of NTS. We evaluate our proposed CNN-based Spatial NTS against three ablations: Global NTS, Local NTS, and Hyper NTS. Global NTS (in Figure 17) is built upon our full model by replacing local texture embedding $e_k(\mathbf{r})$ with global pose θ . Local NTS (in Figure 18) transforms observation UV coordinates $(\hat{U}_t^k(\mathbf{r}), \hat{V}_t^k(\mathbf{r}))$ to canonical UV coordinates $(\hat{U}_t^k(\mathbf{r}), \hat{V}_t^k(\mathbf{r}))$ using a deformation field. Hyper NTS (in Figure 19) adds an ambient MLP to the local-NTS model to model a slicing surface in hyperspace, which yields a coordinate \mathbf{w} in an ambient space.

Table 5 shows the quantitative results on different types of NTS (i.e., global, local, hyper and spatial). It can be seen that the local-NTS model has the worst performance, which is the most limited among these methods. Local NTS only allows coordinate transformation but cannot generate new topological space, which is totally incapable of modeling the topologically varying texture given different poses. As shown in Figure 20, it fails to reconstruct the belt on the pants due to the topological variation ((the belt appears when the performer raises his hand and disappears when he puts his hand down because the shirt covers it).

Since the texture of Global-NTS directly conditions on global pose without restriction, it is easy for Global-NTS to generate a new topological space, as shown in Figure 20, Global-NTS successfully reconstructs the belt on the pants. However, the method that globally models the texture variation is hard to reuse the information of different observation spaces, which leads to ambiguous textures. As shown in Figure 20, the outline of the number 9 on the shirt is not clear and even connected, making it look like an 8. The ambiguous textures are shown in Figure 21, where the number looks more like a red stain. Lack of local mapping makes a relatively poor performance of Global-NTS as demonstrated in Table 5.

Hyper-NTS can model local texture changes by coordi-

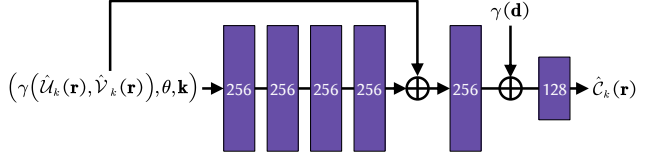


Figure 17. The Global-NTS model directly takes a pose θ as a condition to generate the color. Its architecture is similar to our color MLP M_c (in Figure 14) except for replaces texture embedding $e_k(\mathbf{r})$ with pose θ .

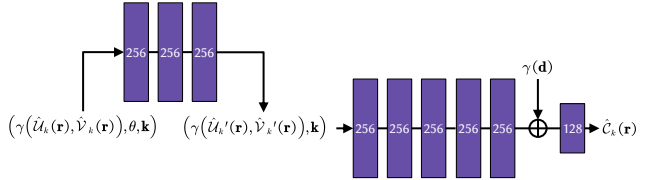


Figure 18. The Local-NTS model transforms UV coordinates $(\hat{U}_t^k(\mathbf{r}), \hat{V}_t^k(\mathbf{r}))$ to $(\hat{U}_t^k(\mathbf{r}), \hat{V}_t^k(\mathbf{r}))$ using a deformation field conditioned on pose θ and modeled by three fully-connected layers of 256 channels. Then we use the transformed UV coordinates, part label vector \mathbf{k} and viewing direction \mathbf{d} as inputs to the subsequent MLP modeled by five fully-connected layers of 256 channels and one fully-connected layer of 128.

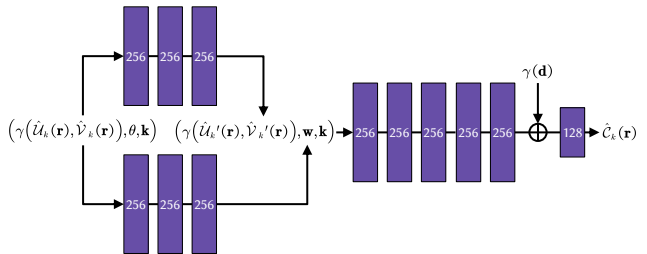


Figure 19. The Hyper-NTS model adds an ambient MLP to the local-NTS model to parameterize the deformation field, which yields warped UV coordinates $(\hat{U}_t^k(\mathbf{r}), \hat{V}_t^k(\mathbf{r}))$ and a coordinate \mathbf{w} in the ambient space. Both outputs, part label vector \mathbf{k} and viewing direction \mathbf{d} , are concatenated to the subsequent MLP to produce view-dependent colors. The ambient MLP has the same architecture as the deformation MLP.

nate transformation and generate new topological spaces simultaneously, so it performs better than Global-NTS and Local-NTS. However, it is a thorny issue to tune the dimension of coordinate \mathbf{w} . If the dimension of the coordinates \mathbf{w} is too high, Hyper-NTS works as Global-NTS, while functioning as Local-NTS if too low.

In contrast, as shown in Table 5, our CNN-based Spatial NTS outperforms all other NTS, which benefits from the nature of convolution operation capturing local 2D texture changes. At the same time, the MLP only needs to model the local mapping between the neural texture stack and RGB color.

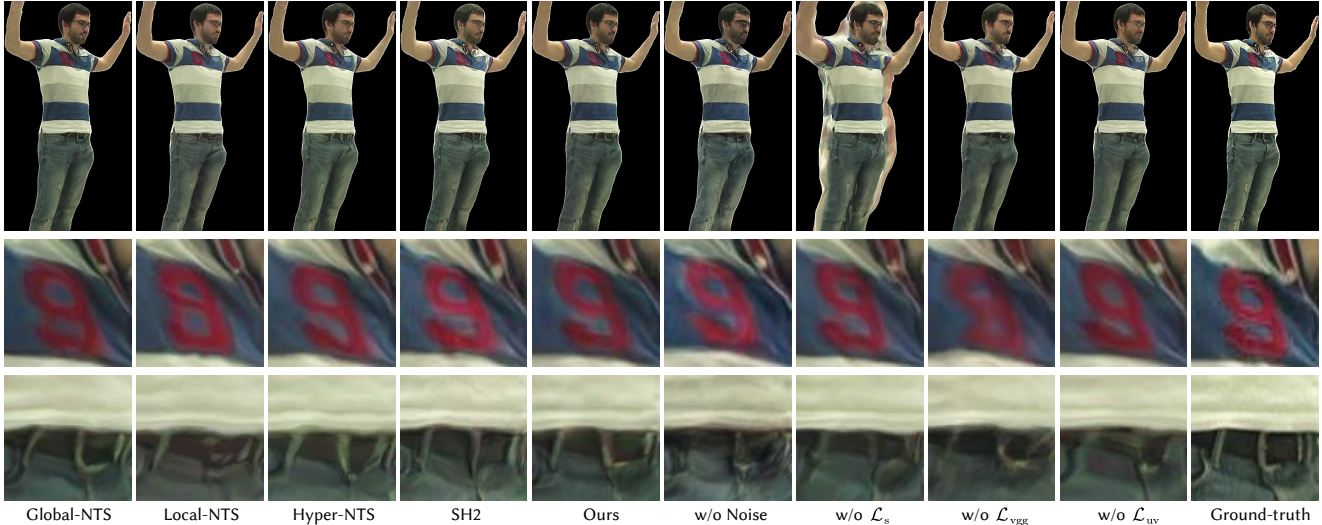


Figure 20. Renderings of our model against ablations.

| Type | Novel View Synthesis | | | Novel Pose Generation | | |
|-------------|----------------------|-------|--------|-----------------------|-------|--------|
| | PSNR↑ | SSIM↑ | LPIPS↓ | PSNR↑ | SSIM↑ | LPIPS↓ |
| Global NTS | 29.86 | 0.966 | 0.062 | 26.18 | 0.927 | 0.074 |
| Local NTS | 29.82 | 0.965 | 0.061 | 26.15 | 0.926 | 0.074 |
| Hyper NTS | 30.08 | 0.966 | 0.059 | 26.19 | 0.927 | 0.073 |
| Spatial NTS | 30.38 | 0.966 | 0.036 | 26.20 | 0.927 | 0.073 |

Table 5. Effects of different types of NTS on our model.

As demonstrated in Figure 20 and Figure 21, our CNN-based Spatial NTS can accurately capture high-frequency details like numbers or wrinkles on shirts, glasses, and a belt on pants.

NTS at Different Resolutions. As shown in Figure 15, we generate an NTS at a resolution of 64×64 . Choosing the resolution of NTS provides a trade-off between quality and memory. We analyze the impacts of resolution in Figure 22, where we report test quality vs. resolution for the dataset of CMU-p2 on PSNR, SSIM and LPIPS metrics. Restricted to memory limitations, NTS has a maximum resolution of 128. It can be observed that the larger resolution of NTS, the better the model performed on novel view synthesis and the novel pose generalization tasks. In this analysis, we found 64×64 to be a favorable optimum in our applications, where NTS at 128×128 resolution is not much better than at 64×64 resolution but costs more memory and time, so we choose 64×64 resolution in all other experiments and recommend it as the default to practitioners.

D.3. View-dependent Color

Ray Direction Noise. To model view-dependent RGB color of human performances, we apply positional encoding $\gamma(\cdot)$ [43] to the viewing direction, and pass the en-

coded viewing direction, UV map and the sampled texture embedding into the color network M_c to decode the view-dependent color $\hat{C}_k(\mathbf{r})$ of camera ray \mathbf{r} .

Since the UV map is generated in a learning-based fashion rather than using direct sampling locations, the color network tends to overfit training viewing directions directly sampled during training. To improve the generalisability of the color network, we apply a sub-pixel noise to the ray direction. Here, instead of shooting in the pixel centers, a noise ψ is used as follows:

$$x_i = \mathbf{o} + t_i(\mathbf{d} + \psi), \quad (15)$$

where noise ψ can be interpreted as a locality condition, i.e., in similar view conditions, RGB color should not be too different. It allows the model to learn smoother transitions between different views.

The ablation of ours w/o noise is presented in Table 6 and demonstrates the effectiveness of the proposed ray direction noise. Figure 20 and Figure 21 show qualitative results of ours w/o noise tests on the novel views. Obviously, ours w/o noise tends to exhibit artifacts in the rendering and textures.

Spherical Harmonic Functions. Another way to reconstruct the view-dependent color of human performance is using the spherical harmonic (SH) functions. We pass the encoded UV map with the sampled texture embedding into the color network M_c to decode spherical harmonic coefficients η for each color channel:

$$(\hat{\eta}_k^0(\mathbf{r}), \hat{\eta}_k^1(\mathbf{r}), \dots, \hat{\eta}_k^n(\mathbf{r})) = M_c\left(\gamma(\hat{\mathcal{U}}_k(\mathbf{r}), \hat{\mathcal{V}}_k(\mathbf{r})), \mathbf{e}_k(\mathbf{r}), \mathbf{k}\right), \quad (16)$$

where spherical harmonics $(\eta^0, \eta^1, \dots, \eta^n)$ form an orthogonal basis for functions defined over the sphere, with

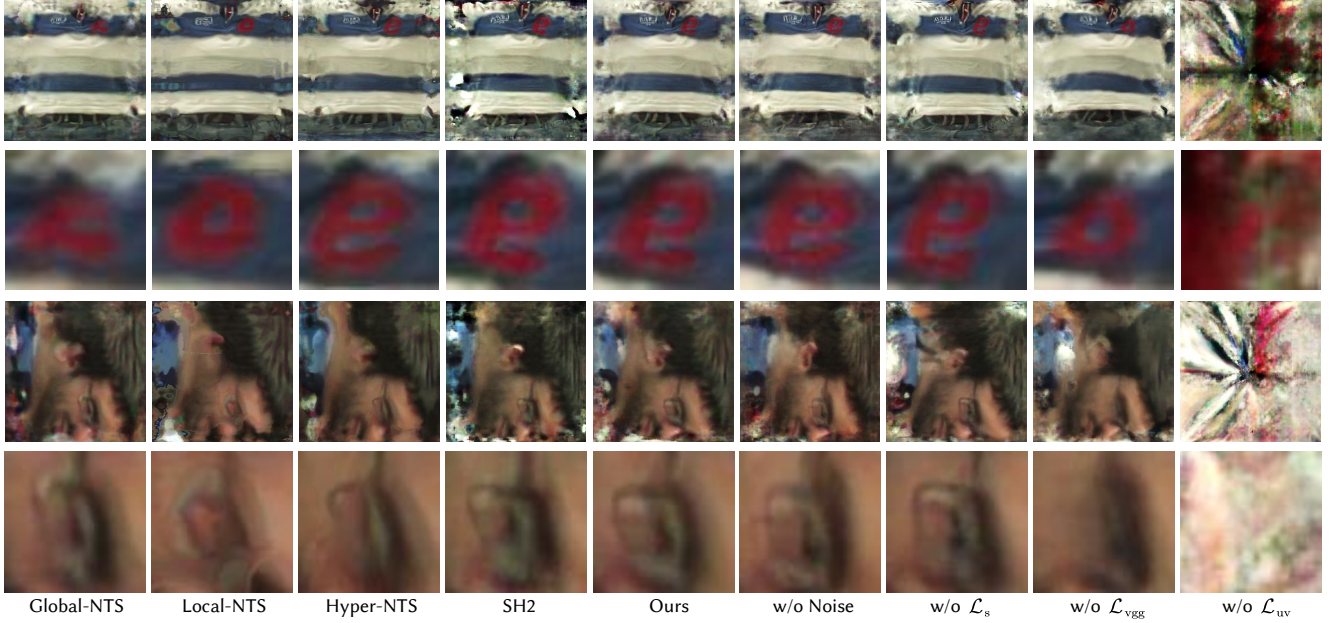


Figure 21. Textures of our model against ablations.

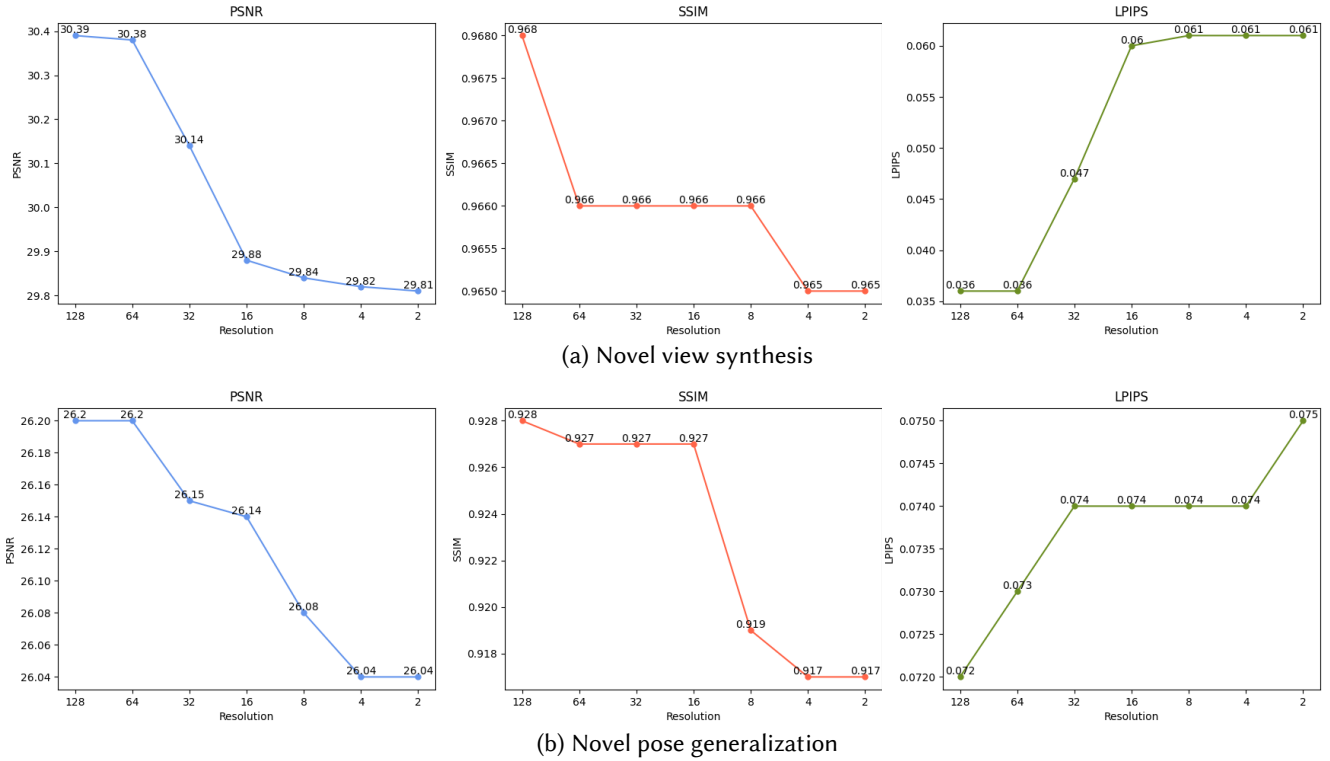


Figure 22. Impacts of NTS at different resolutions.

zero degree harmonics η^0 encoding diffuse color and higher degree harmonics encoding specular effects. The view-dependent color $\hat{C}_k(\mathbf{r})$ of camera ray \mathbf{r} can be determined by querying the specular spherical functions SH at desired

viewing direction \mathbf{d} :

$$\hat{C}_k(\mathbf{r}) = S \left(\frac{\hat{\eta}_k^0(\mathbf{r})}{2} \sqrt{\frac{1}{\pi}} + \sum_{m=1}^n SH^m(\hat{\eta}_k^m(\mathbf{r}), \mathbf{d}) \right), \quad (17)$$

| Type | Novel view synthesis | | | Novel pose generation | | |
|-----------|----------------------|-----------------|--------------------|-----------------------|-----------------|--------------------|
| | PSNR \uparrow | SSIM \uparrow | LPIPS \downarrow | PSNR \uparrow | SSIM \uparrow | LPIPS \downarrow |
| SH1 | 29.41 | 0.966 | 0.052 | 26.00 | 0.926 | 0.078 |
| SH2 | 30.02 | 0.966 | 0.051 | 26.15 | 0.927 | 0.076 |
| SH3 | 29.43 | 0.965 | 0.051 | 26.14 | 0.926 | 0.075 |
| SH4 | 27.83 | 0.962 | 0.054 | 26.10 | 0.926 | 0.076 |
| w/o noise | 28.56 | 0.962 | 0.058 | 25.90 | 0.924 | 0.078 |
| Ours | 30.38 | 0.966 | 0.036 | 26.20 | 0.927 | 0.073 |

Table 6. Comparison of different methods to model the view-dependent RGB color.

where S is the sigmoid function for normalizing the colors.

A higher degree of harmonics results in a higher capability to model high-frequency color but is more prone to overfit the training viewing direction.

The ablation of different harmonics degrees is presented in Table 6, which demonstrates that the harmonics degree of 2 model achieves the best performance among all the SH models but still cannot reach the performance of ours. Figure 20 illustrates the qualitative results of SH2 tests on the novel views, which shows that SH2 suffers from global color shifts (head of the performer) and artifacts (the belt on pants), while ours does not.

D.4. Video Frames and Input Views

To analyze the impacts of the number of camera views and video length, we show the results of our models trained with different numbers of camera views and video frames in Table 7. We conduct the experiments on performer 313 of the ZJU dataset. All the results are evaluated on the rest two views of the first 60-frame video. The results show that although the number of training views improves the performance on novel view synthesis, sparse four views are good enough for our model to reconstruct dynamic human performances. In addition, the ablation study of frame numbers indicates that training on too many frames may decrease the performance as the network cannot fit such a long video, which is also mentioned in NeuralBody [41].

E. Additional Results

E.1. Novel View Synthesis

For comparison, we synthesize images of training poses in hold-out test-set views. More qualitative results of novel view synthesis are shown in Figure 23, Figure 24 and Figure 25. Our method produces photo-realistic images with sharp details, particularly letters on clothes (in Figure 23), stripes on T-shirts, and wrinkles in clothes (in Figure 24), which benefits from our proposed Spatial NTS that encodes high-frequency appearance information.

Figure 25 shows the results of comparisons on ZJU Mo-

| Task | 4 Views | | | 20 Views | | |
|-------------|-----------------|-----------------|--------------------|-----------------|-----------------|--------------------|
| | PSNR \uparrow | SSIM \uparrow | LPIPS \downarrow | PSNR \uparrow | SSIM \uparrow | LPIPS \downarrow |
| 60 Frames | 29.56 | 0.967 | 0.045 | 31.12 | 0.975 | 0.038 |
| 300 Frames | 29.23 | 0.963 | 0.048 | 29.90 | 0.968 | 0.046 |
| 600 Frames | 29.37 | 0.964 | 0.049 | 29.50 | 0.966 | 0.048 |
| 1200 Frames | 28.96 | 0.961 | 0.052 | 29.26 | 0.963 | 0.053 |

Table 7. Ablation study on the number of training frames and views.

cap and H36M dataset, which are trained on sparse-views video sequences. Here, we use four training views on ZJU Mocap dataset and three for the most challenging H36M dataset. Our model obviously performs much better in details and sharpness than all other baselines. Furthermore, DyNeRF fails to render plausible results with sparse training views because taking time-varying latent codes as the conditions are hard to reuse information among frames.

E.2. Novel View Synthesis of Dynamic Humans

We present more results on novel view synthesis of dynamic humans in Figure 26. As presented, our model can handle a dynamic human with rich textures and challenging motions, and preserve sharp image details like letters and wrinkles, while keeping inter-view and inter-frame consistency. Note that the last row is the result of our model on the H36M dataset, demonstrating that our model can still recover high-fidelity free-view videos under sparse training views.

In addition, we show the intermediate UV images and final RGB images rendered by our model varying with views and human poses in Figure 27, which demonstrates that our model can synthesize photo-realistic view-consistent RGB images that condition on view-consistent UV images rendered by UV volumes.

E.3. Novel Pose Generalization

More qualitative results of novel pose generalization are shown in Figure 28 and Figure 29, where the latter are the results of comparisons on H36M dataset where only three cameras are available for training.

E.4. Reshaping

By changing the SMPL parameters, we can conveniently deform the human performer. We present the performer whose size is getting smaller and the shoulder-to-waist ratio is getting smaller from left to right in Figure 30. With the help of view-consistent UV coordinates generated by UV volumes, our model still renders view-consistent images with challenging shape parameters. These rendered images maintain high appearance consistency across changing shapes thanks to the neural texture stacks.

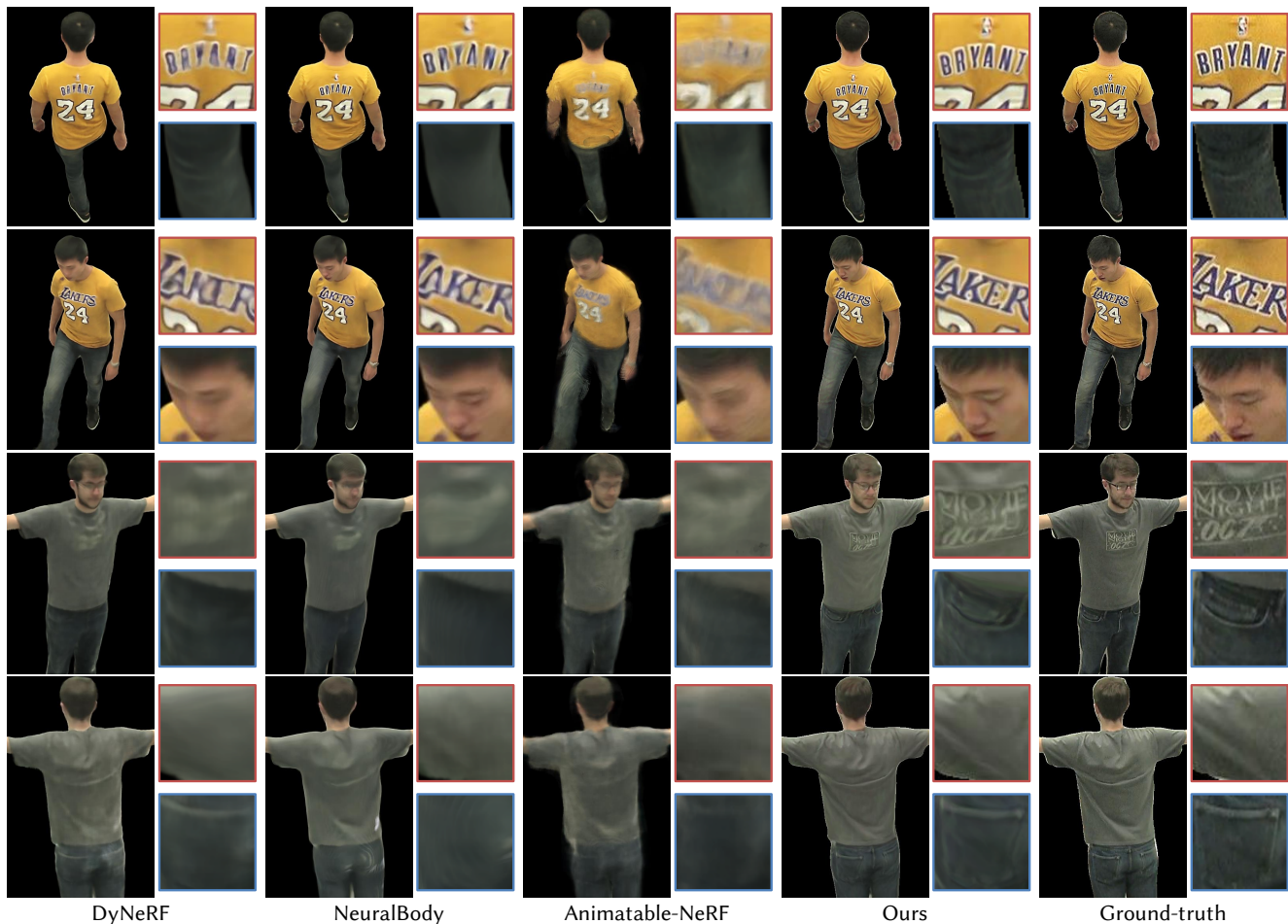


Figure 23. Comparisons on test-set views for performers from CMU Panoptic dataset with 960×540 images. Our model generates photo-realistic appearance images even with rich textures, particularly letters on the performers’ clothes. By contrast, baselines give blurry results while missing a lot of high-frequency details. Here, we present results on two different test views at the same time for each performer.

E.5. Visualization of NTS

In contrast to [41] learning a radiance field in the 3D volumes, we decompose a 3D dynamic human into 3D UV volumes and 2D neural texture stacks, as illustrated in Figure 31. The disentanglement of appearance from geometry enables us to achieve real-time rendering of free-view human performance. We learn a view-consistent UV field to transfer neural texture embeddings to colors, which guarantees view-consistent human performance. Details like the folds of clothing vary from motion to motion, as does the topology, so we require a dynamic texture representation. Referring to Figure 32, we visualize the pose-driven neural texture stacks to describe appearance at different times, which enables us to handle dynamic 3D reconstruction tasks and to generalize our model to unseen poses. It is obvious that our learned NTS preserve rich textures and high-frequency details varying from different poses.

E.6. Retexturing

With the learned dense correspondence of 3D UV volumes and 2D neural texture stacks, we can edit performers’ 3D cloth with user-provided 2D textures. As shown in Figure 33, given arbitrary artistic paintings, we can produce cool stylized dynamic humans leveraging stylizations transferred from the original texture stacks by the network [12]. Visually inspected, the new texture is well painted onto the performer’s T-shirt under different poses at different viewing directions. Besides, we perform some interesting applications of our model in Figure 34 and Figure 35, which include a 3D virtual try-on implemented by replacing original texture stacks with a user-provided appearance. The visualization results demonstrate that our model can conveniently edit textures preserving the rich appearance and various styles, which benefits from our proposed Neural Texture Stacks, and can render retextured human performance with view consistency well using 3D UV volumes.

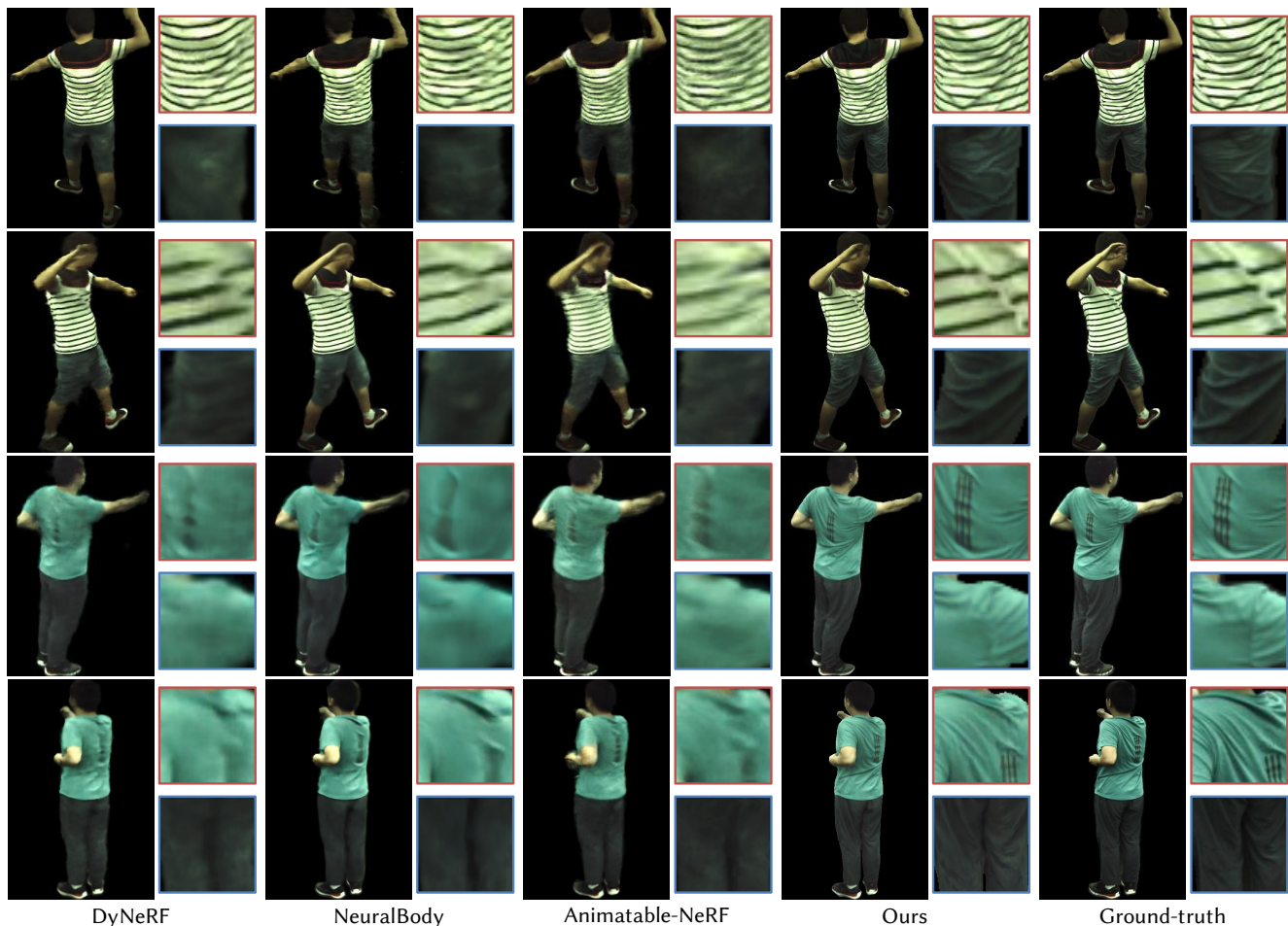


Figure 24. Comparisons on test-set views for performers from the ZJU Mocap dataset. Our model obviously performs well in details (e.g., stripes on T-shirts and wrinkles in clothes) and sharpness than all other baselines, which benefits from our proposed Spatial NTS that encodes high-frequency appearance information. Other methods give plausible but blurry and rough synthesized images. Here, we present results on two different test views at the same time for each performer.

References

- [1] Timur Bagautdinov, Chenglei Wu, Tomas Simon, Fabian Prada, Takaaki Shiratori, Shih-En Wei, Weipeng Xu, Yaser Sheikh, and Jason Saragih. Driving-signal aware full-body avatars. *ACM Transactions on Graphics (TOG)*, 40(4):1–17, 2021. 2
- [2] Chris Buehler, Michael Bosse, Leonard McMillan, Steven Gortler, and Michael Cohen. Unstructured lumigraph rendering. In *Proceedings of the 28th annual conference on Computer graphics and interactive techniques*, pages 425–432, 2001. 2
- [3] Xu Chen, Yufeng Zheng, Michael J Black, Otmar Hilliges, and Andreas Geiger. Snarf: Differentiable forward skinning for animating non-rigid neural implicit shapes. In *Proceedings of the IEEE International Conference on Computer Vision*, 2021. 3
- [4] Alvaro Collet, Ming Chuang, Pat Sweeney, Don Gillett, Dennis Evseev, David Calabrese, Hugues Hoppe, Adam Kirk, and Steve Sullivan. High-quality streamable free-viewpoint video. *ACM Transactions on Graphics (TOG)*, 34(4):1–13, 2015. 1
- [5] Alvaro Collet, Ming Chuang, Pat Sweeney, Don Gillett, Dennis Evseev, David Calabrese, Hugues Hoppe, Adam Kirk, and Steve Sullivan. High-quality streamable free-viewpoint video. *ACM Transactions on Graphics (TOG)*, 34(4):1–13, 2015. 2
- [6] Abe Davis, Marc Levoy, and Fredo Durand. Unstructured light fields. In *Computer Graphics Forum*, volume 31, pages 305–314, 2012. 2
- [7] Martin Eisemann, Bert De Decker, Marcus Magnor, Philippe Bekaert, Edilson De Aguiar, Naveed Ahmed, Christian Theobalt, and Anita Sellent. Floating textures. In *Computer graphics forum*, volume 27, pages 409–418, 2008. 2
- [8] John Flynn, Michael Broxton, Paul Debevec, Matthew DuVall, Graham Fyffe, Ryan Overbeck, Noah Snavely, and Richard Tucker. Deepview: View synthesis with learned gradient descent. In *Proceedings of the IEEE/CVF Conference*

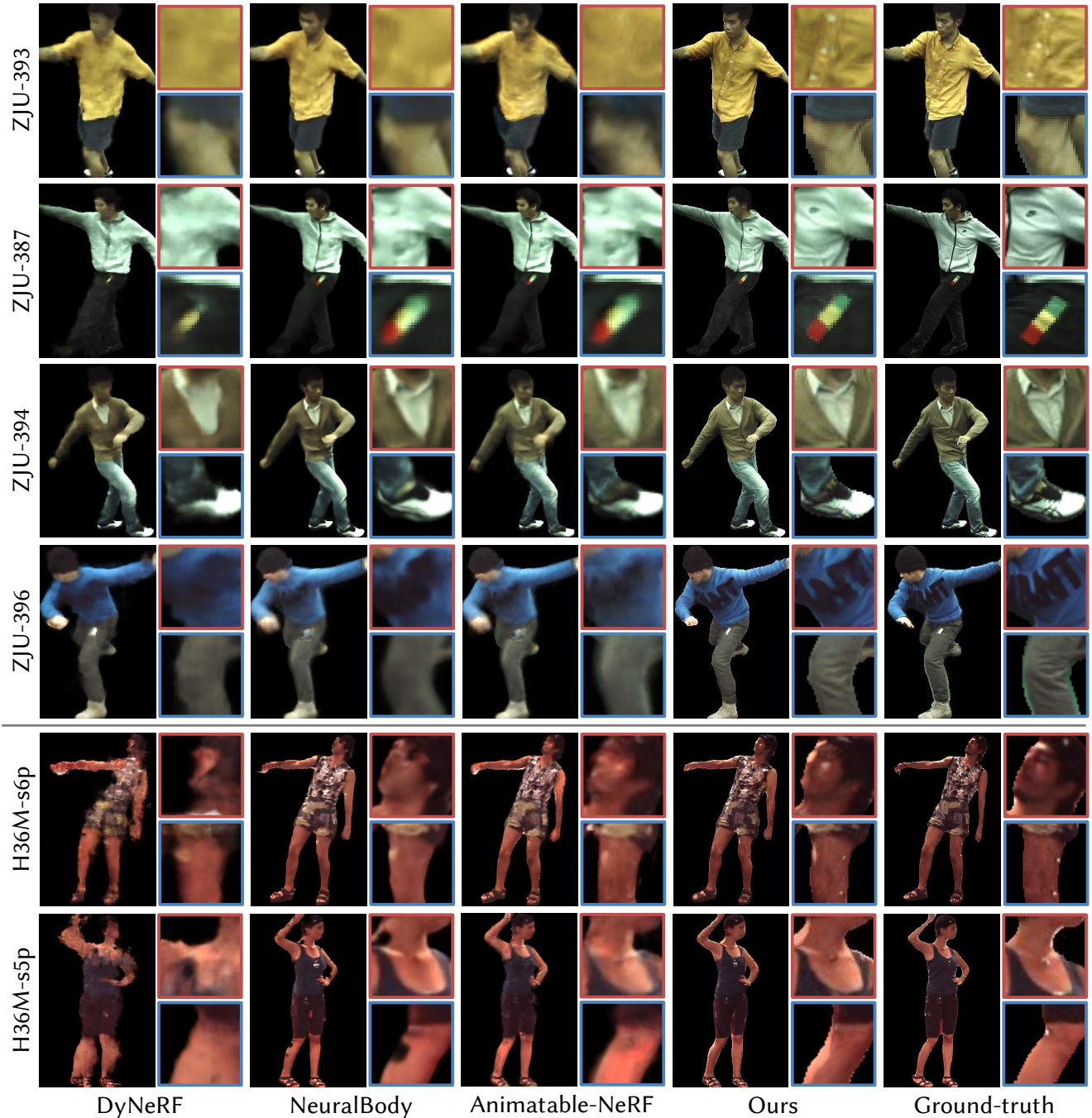


Figure 25. Comparisons on test-set views from ZJU Mocap dataset with four training views and the most challenging H36M dataset with only three available views for training. Our model generates high-definition results even with rich textures and challenging motions. DyNeRF fails to render plausible results with sparse training views because taking time-varying latent codes as the conditions are hard to reuse information among frames.

on *Computer Vision and Pattern Recognition*, pages 2367–2376, 2019. 2

- [9] Sara Fridovich-Keil, Alex Yu, Matthew Tancik, Qinhong Chen, Benjamin Recht, and Angjoo Kanazawa. Plenoxels: Radiance fields without neural networks. In *Proceedings of*

the IEEE/CVF Conference on Computer Vision and Pattern Recognition, pages 5501–5510, 2022. 2

- [10] Stephan J Garbin, Marek Kowalski, Matthew Johnson, Jamie Shotton, and Julien Valentin. Fastnerf: High-fidelity neural rendering at 200fps. In *Proceedings of the IEEE/CVF In-*



Figure 26. The rendering of our method on different sequences. Our model can handle a dynamic human with rich textures and challenging motions preserving sharp image details like letters and wrinkles, which benefits from our proposed Spatial NTS that encodes high-frequency appearance information while keeping inter-view and inter-frame consistency, which benefits from our proposed *UV Volumes*. Note that the last row is the result of our model on the H36M dataset, which demonstrates that our model can still recover high-fidelity free-view videos under sparse training views.



Figure 27. Novel view synthesis of the dynamic human. Our model can synthesize photo-realistic view-consistent RGB images condition on view-consistent UV images rendered by UV volumes. Here, The horizontal axis shows the change in novel views and, the vertical axis shows the change in human poses. All results are rendered from novel views in the training pose sequence.

ternational Conference on Computer Vision, pages 14346–14355, 2021. 2

- [11] Leon A Gatys, Alexander S Ecker, and Matthias Bethge. Image style transfer using convolutional neural networks. In *Proceedings of the IEEE/CVF Conference on Computer Vision and Pattern Recognition*, pages 2414–2423, 2016. 5
- [12] Golnaz Ghiasi, Honglak Lee, Manjunath Kudlur, Vincent Dumoulin, and Jonathon Shlens. Exploring the structure of

a real-time, arbitrary neural artistic stylization network. In *Proceedings of the British Machine Vision Conference*, pages 114.1–114.12, 2017. 7, 15

- [13] Ke Gong, Xiaodan Liang, Yicheng Li, Yimin Chen, Ming Yang, and Liang Lin. Instance-level human parsing via part grouping network. In *Proceedings of the European Conference on Computer Vision*, pages 770–785, 2018. 6
- [14] Steven J Gortler, Radek Grzeszczuk, Richard Szeliski, and

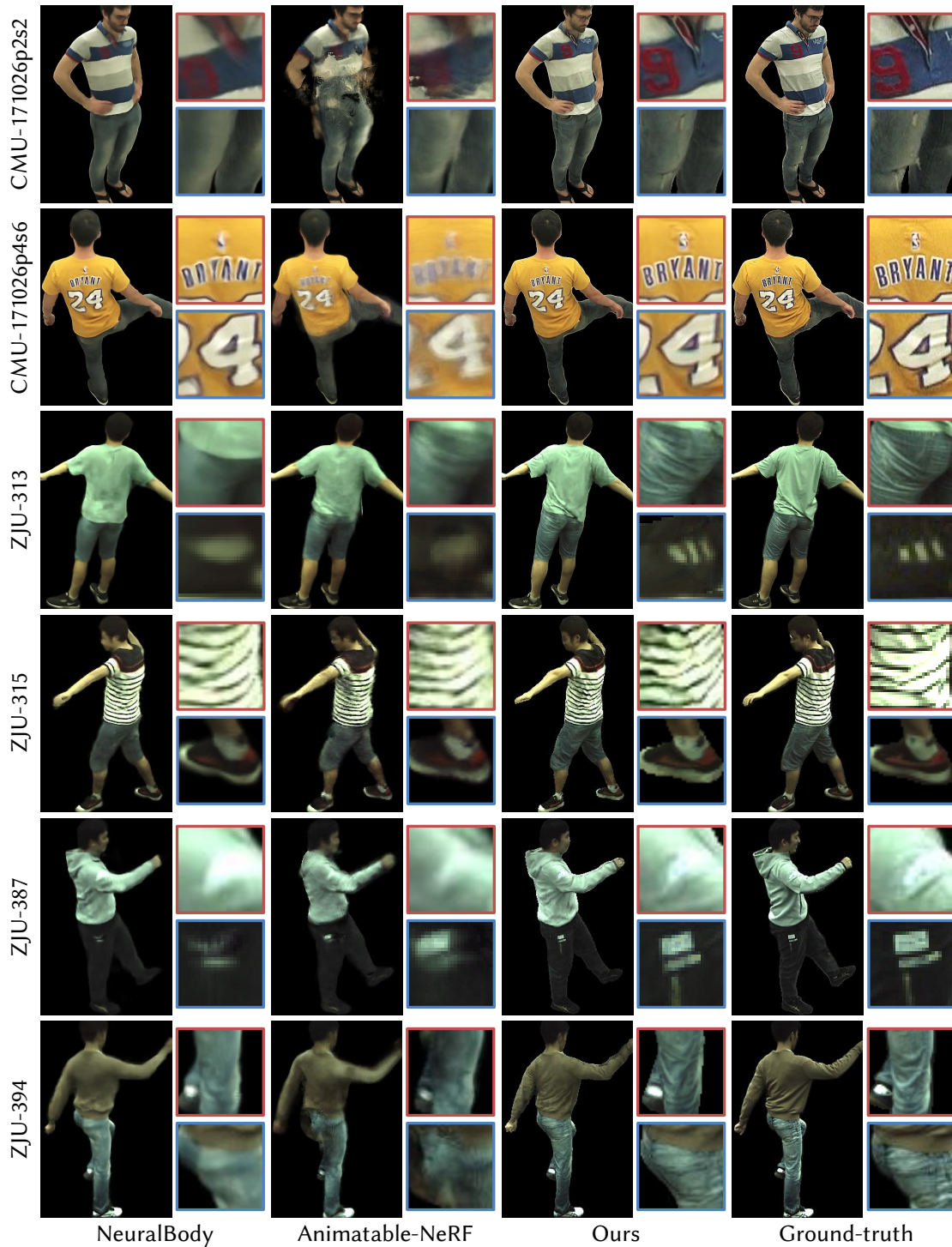


Figure 28. Comparisons on test-set poses for performers from CMU Panoptic and ZJU Mocap dataset.

Michael F Cohen. The lumigraph. In *Proceedings of the conference on Computer graphics and interactive techniques*, pages 43–54, 1996. 2

[15] Rıza Alp Güler, Natalia Neverova, and Iasonas Kokkinos. Denspose: Dense human pose estimation in the wild. In

Proceedings of the IEEE/CVF Conference on Computer Vision and Pattern Recognition, pages 7297–7306, 2018. 3

[16] Rıza Alp Güler, Natalia Neverova, and Iasonas Kokkinos. Denspose: Dense human pose estimation in the wild. In *Proceedings of the IEEE/CVF Conference on Computer Vi-*

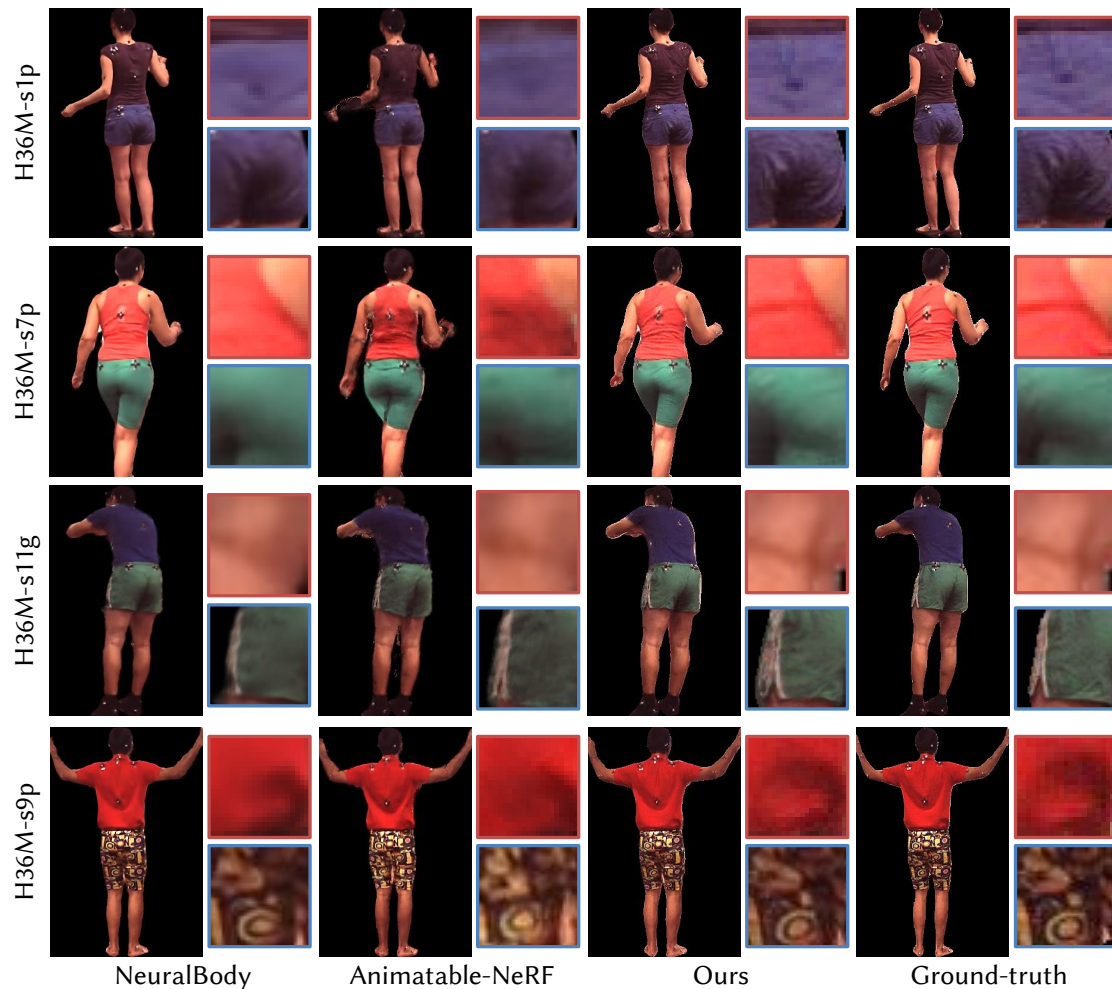


Figure 29. Comparisons on test-set poses for performers from the most challenging H36M dataset.

- sion and Pattern Recognition*, pages 7297–7306, 2018. 9
- [17] Peter Hedman, Julien Philip, True Price, Jan-Michael Frahm, George Drettakis, and Gabriel Brostow. Deep blending for free-viewpoint image-based rendering. *ACM Transactions on Graphics (TOG)*, 37(6):1–15, 2018. 2
- [18] Peter Hedman, Pratul P Srinivasan, Ben Mildenhall, Jonathan T Barron, and Paul Debevec. Baking neural radiance fields for real-time view synthesis. In *Proceedings of the IEEE/CVF International Conference on Computer Vision*, pages 5875–5884, 2021. 2
- [19] Catalin Ionescu, Dragos Papava, Vlad Olaru, and Cristian Sminchisescu. Human3. 6m: Large scale datasets and predictive methods for 3d human sensing in natural environments. *IEEE transactions on pattern analysis and machine intelligence*, 36(7):1325–1339, 2013. 6
- [20] Max Jaderberg, Karen Simonyan, Andrew Zisserman, et al. Spatial transformer networks. *Advances in neural information processing systems*, 28:2017–2025, 2015. 4
- [21] Justin Johnson, Alexandre Alahi, and Li Fei-Fei. Perceptual losses for real-time style transfer and super-resolution. In *European conference on computer vision*, pages 694–711. Springer, 2016. 5
- [22] Hanbyul Joo, Tomas Simon, Xulong Li, Hao Liu, Lei Tan, Lin Gui, Sean Banerjee, Timothy Godisart, Bart Nabbe, Iain Matthews, et al. Panoptic studio: A massively multiview system for social interaction capture. *IEEE transactions on pattern analysis and machine intelligence*, 41(1):190–204, 2017. 6
- [23] James T Kajiya and Brian P Von Herzen. Ray tracing volume densities. *Proceedings of the Conference on Computer Graphics and Interactive Techniques*, 18(3):165–174, 1984. 4
- [24] Nima Khademi Kalantari, Ting-Chun Wang, and Ravi Ramamoorthi. Learning-based view synthesis for light field cameras. *ACM Transactions on Graphics (TOG)*, 35(6):1–10, 2016. 2
- [25] Diederik P Kingma and Jimmy Ba. Adam: A method for stochastic optimization. *arXiv preprint arXiv:1412.6980*, 2014. 10
- [26] Marc Levoy and Pat Hanrahan. Light field rendering. In *Pro-*



Figure 30. Novel view synthesis results of reshaping. By changing the SMPL parameters, we can conveniently deform the human performer. We present the performer whose size is getting smaller and the shoulder-to-waist ratio is getting smaller from left to right. With the help of view-consistent UV coordinates encoded by UV volumes, our model still renders view-consistent images with challenging shape parameters. Here, The horizontal axis shows shape changes and the vertical axis shows view changes. All results are rendered from novel views.

ceedings of the conference on Computer graphics and interactive techniques, pages 31–42, 1996. 2

[27] Tianye Li, Mira Slavcheva, Michael Zollhoefer, Simon Green, Christoph Lassner, Changil Kim, Tanner Schmidt, Steven Lovegrove, Michael Goesele, Richard Newcombe, et al. Neural 3d video synthesis from multi-view video. In *Proceedings of the IEEE/CVF Conference on Computer Vi-*

sion and Pattern Recognition, pages 5521–5531, 2022. 2, 6, 10

[28] Zhengqi Li, Simon Niklaus, Noah Snavely, and Oliver Wang. Neural scene flow fields for space-time view synthesis of dynamic scenes. In *Proceedings of the IEEE/CVF Conference on Computer Vision and Pattern Recognition*, pages 6498–6508, 2021. 3



Figure 31. We decompose (a) the dynamic human into (b) 3D UV volumes and (c) 2D neural texture stacks. The disentanglement of appearance from geometry enables us to achieve real-time rendering of free-view human performance. We show performers and their UV avatars with four different poses at four different viewing directions from CMU Panoptic, ZJU-Mocap and H36M datasets. Their neural texture stacks that preserve human appearance with high-frequency details under one of these poses are visualized in the last column. Our method takes smooth UV coordinates to sample neural texture stacks for corresponding RGB value.

[29] Lingjie Liu, Jiatao Gu, Kyaw Zaw Lin, Tat-Seng Chua, and Christian Theobalt. Neural sparse voxel fields. *Advances in Neural Information Processing Systems*, 33:15651–15663, 2020. 2

Sarkar, Jiatao Gu, and Christian Theobalt. Neural actor: Neural free-view synthesis of human actors with pose control. *ACM Transactions on Graphics (TOG)*, 40(6):1–16, 2021. 3

[30] Lingjie Liu, Marc Habermann, Viktor Rudnev, Kripasindhu

[31] Stephen Lombardi, Tomas Simon, Jason Saragih, Gabriel

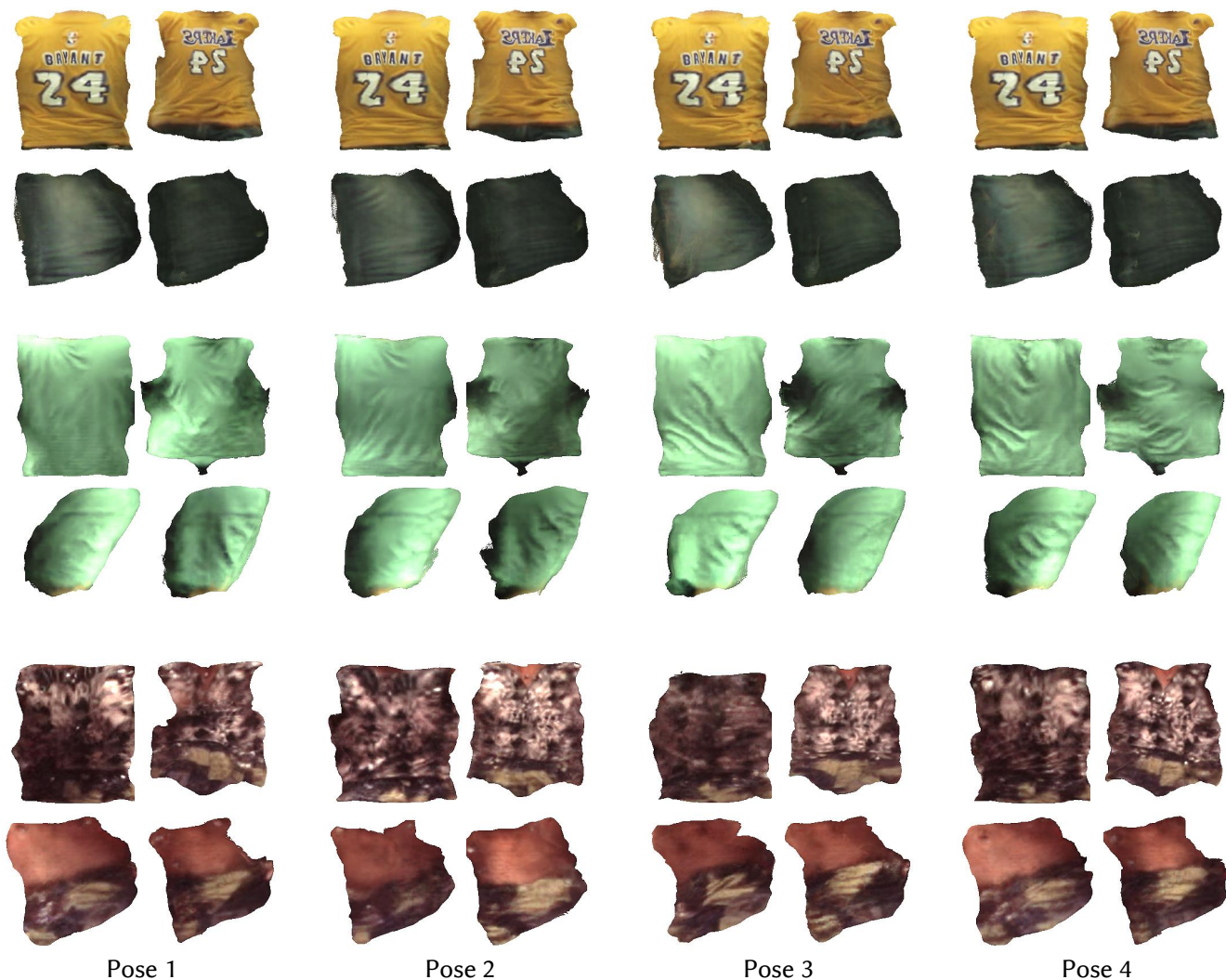


Figure 32. Visualization of neural texture stacks under different poses. Details like the folds of clothing vary from motion to motion, as does the topology. Therefore, we propose pose-driven neural texture stacks to describe textures at different times, which enables us to handle dynamic 3D reconstruction tasks and to generalize our model to unseen poses.

- Schwartz, Andreas Lehrmann, and Yaser Sheikh. Neural volumes: learning dynamic renderable volumes from images. *ACM Transactions on Graphics (TOG)*, 38(4):1–14, 2019. 2
- [32] Stephen Lombardi, Tomas Simon, Gabriel Schwartz, Michael Zollhoefer, Yaser Sheikh, and Jason Saragih. Mixture of volumetric primitives for efficient neural rendering. *ACM Transactions on Graphics (TOG)*, 40(4):1–13, 2021. 3
- [33] Shugao Ma, Tomas Simon, Jason Saragih, Dawei Wang, Yuecheng Li, Fernando De La Torre, and Yaser Sheikh. Pixel codec avatars. In *Proceedings of the IEEE/CVF Conference on Computer Vision and Pattern Recognition*, pages 64–73, 2021. 2
- [34] Ben Mildenhall, Pratul P Srinivasan, Rodrigo Ortiz-Cayon, Nima Khademi Kalantari, Ravi Ramamoorthi, Ren Ng, and Abhishek Kar. Local light field fusion: Practical view synthesis with prescriptive sampling guidelines. *ACM Transactions on Graphics (TOG)*, 38(4):1–14, 2019. 2
- [35] Ben Mildenhall, Pratul P Srinivasan, Matthew Tancik, Jonathan T Barron, Ravi Ramamoorthi, and Ren Ng. Nerf: Representing scenes as neural radiance fields for view synthesis. In *European conference on computer vision*, pages 405–421. Springer, 2020. 1, 2, 3, 5
- [36] Armin Mustafa, Hansung Kim, Jean-Yves Guillemaut, and Adrian Hilton. Temporally coherent 4d reconstruction of complex dynamic scenes. In *Proceedings of the IEEE/CVF Conference on Computer Vision and Pattern Recognition*, pages 4660–4669, 2016. 2
- [37] Michael Niemeyer and Andreas Geiger. Giraffe: Representing scenes as compositional generative neural feature fields. In *Proceedings of the IEEE/CVF Conference on Computer Vision and Pattern Recognition*, pages 11453–11464, 2021. 2



Style

Retextured 3D human

Style

Retextured 3D human

Figure 33. Our model supports rendering a stylized dynamic human with arbitrary artistic painting, which can be applied in controllable 3D style transfer with multi-view consistency.

[38] Keunhong Park, Utkarsh Sinha, Jonathan T Barron, Sofien Bouaziz, Dan B Goldman, Steven M Seitz, and Ricardo Martin-Brualla. Nerfies: Deformable neural radiance fields. In *Proceedings of the IEEE/CVF International Conference on Computer Vision*, pages 5865–5874, 2021. 2, 3

Barron, Sofien Bouaziz, Dan B Goldman, Ricardo Martin-Brualla, and Steven M Seitz. Hypernerf: a higher-dimensional representation for topologically varying neural radiance fields. *ACM Transactions on Graphics (TOG)*, 40(6):1–12, 2021. 2, 3

[39] Keunhong Park, Utkarsh Sinha, Peter Hedman, Jonathan T

[40] Sida Peng, Junting Dong, Qianqian Wang, Shangzhan

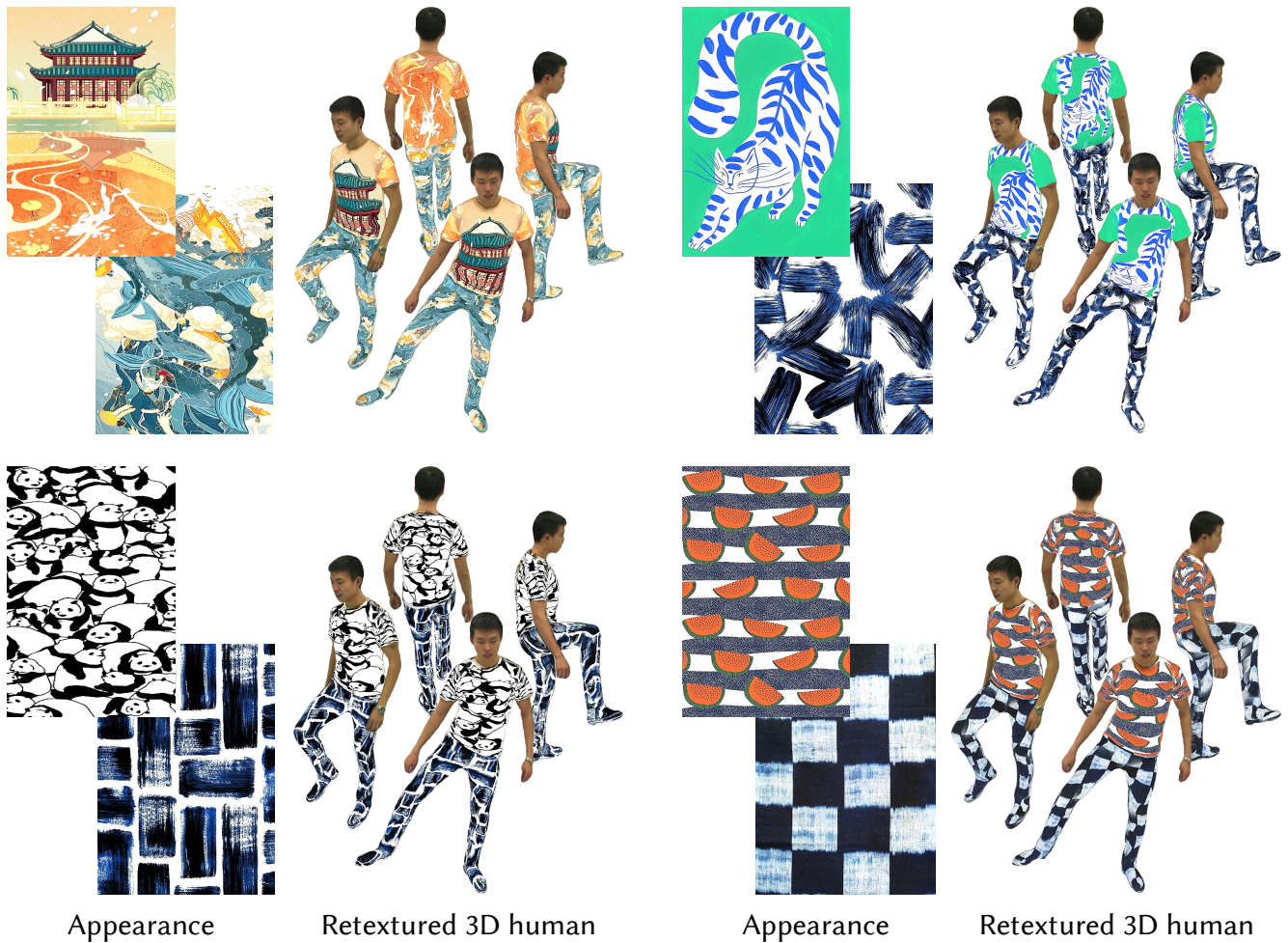


Figure 34. Our model allows us to generate free-view human performance with a user-provided cloth texture image, which enables some interesting applications such as real-time 3D virtual try-on. We collect these appearance images from the Internet.

- Zhang, Qing Shuai, Xiaowei Zhou, and Hujun Bao. Animatable neural radiance fields for modeling dynamic human bodies. In *Proceedings of the IEEE International Conference on Computer Vision*, 2021. [3](#), [6](#), [10](#)
- [41] Sida Peng, Yuanqing Zhang, Yinghao Xu, Qianqian Wang, Qing Shuai, Hujun Bao, and Xiaowei Zhou. Neural body: Implicit neural representations with structured latent codes for novel view synthesis of dynamic humans. In *Proceedings of the IEEE/CVF Conference on Computer Vision and Pattern Recognition*, pages 9054–9063, 2021. [2](#), [5](#), [6](#), [8](#), [9](#), [10](#), [14](#), [15](#)
- [42] Albert Pumarola, Enric Corona, Gerard Pons-Moll, and Francesc Moreno-Noguer. D-nerf: Neural radiance fields for dynamic scenes. In *Proceedings of the IEEE/CVF Conference on Computer Vision and Pattern Recognition*, pages 10318–10327, 2021. [2](#), [3](#)
- [43] Nasim Rahaman, Aristide Baratin, Devansh Arpit, Felix Draxler, Min Lin, Fred Hamprecht, Yoshua Bengio, and Aaron Courville. On the spectral bias of neural networks. In *International Conference on Machine Learning*, pages 5301–5310, 2019. [4](#), [12](#)
- [44] Christian Reiser, Songyou Peng, Yiyi Liao, and Andreas Geiger. Kilonerf: Speeding up neural radiance fields with thousands of tiny mlps. In *Proceedings of the IEEE/CVF International Conference on Computer Vision*, pages 14335–14345, 2021. [2](#)
- [45] Edoardo Remelli, Timur Bagautdinov, Shunsuke Saito, Chenglei Wu, Tomas Simon, Shih-En Wei, Kaiwen Guo, Zhe Cao, Fabian Prada, Jason Saragih, et al. Drivable volumetric avatars using texel-aligned features. In *ACM SIGGRAPH 2022 Conference Proceedings*, pages 1–9, 2022. [3](#)
- [46] Ruizhi Shao, Hongwen Zhang, He Zhang, Mingjia Chen, Yan-Pei Cao, Tao Yu, and Yebin Liu. Doublefield: Bridging the neural surface and radiance fields for high-fidelity human reconstruction and rendering. In *Proceedings of the IEEE/CVF Conference on Computer Vision and Pattern Recognition*, pages 15872–15882, 2022. [3](#)
- [47] Aliaksandra Shysheya, Egor Zakharov, Kara-Ali Aliev, Renat Bashirov, Egor Burkov, Karim Isakov, Aleksei Ivakhnenko, Yuri Malkov, Igor Pasechnik, Dmitry Ulyanov,



Retextured 3D human

Appearance

Retextured 3D human

Appearance

Figure 35. Our model allows us to generate free-view human performance with a user-provided cloth texture image, which enables some interesting applications such as real-time 3D virtual try-on. We collect these appearance images from the Internet.

- et al. Textured neural avatars. In *Proceedings of the IEEE/CVF Conference on Computer Vision and Pattern Recognition*, pages 2387–2397, 2019. 3
- [48] Karen Simonyan and Andrew Zisserman. Very deep convolutional networks for large-scale image recognition. In *International Conference on Learning Representations*, 2015. 5
- [49] Pratul P Srinivasan, Richard Tucker, Jonathan T Barron, Ravi Ramamoorthi, Ren Ng, and Noah Snavely. Pushing the boundaries of view extrapolation with multiplane images. In *Proceedings of the IEEE/CVF Conference on Computer Vision and Pattern Recognition*, pages 175–184, 2019. 2
- [50] Jingxiang Sun, Xuan Wang, Yichun Shi, Lizhen Wang, Jue Wang, and Yebin Liu. Ide-3d: Interactive disentangled editing for high-resolution 3d-aware portrait synthesis. *ACM Transactions on Graphics (TOG)*, 41(6):1–10, 2022. 2
- [51] Jingxiang Sun, Xuan Wang, Yong Zhang, Xiaoyu Li, Qi Zhang, Yebin Liu, and Jue Wang. Fenerf: Face editing in neural radiance fields. In *Proceedings of the IEEE/CVF Conference on Computer Vision and Pattern Recognition*, pages 7672–7682, 2022. 2
- [52] Justus Thies, Michael Zollhöfer, and Matthias Nießner. Deferred neural rendering: Image synthesis using neural textures. *ACM Transactions on Graphics (TOG)*, 38(4):1–12, 2019. 2
- [53] Edgar Tretschk, Ayush Tewari, Vladislav Golyanik, Michael Zollhöfer, Christoph Lassner, and Christian Theobalt. Non-rigid neural radiance fields: Reconstruction and novel view synthesis of a dynamic scene from monocular video. In *Proceedings of the IEEE/CVF International Conference on Computer Vision*, pages 12959–12970, 2021. 3
- [54] Dmitry Ulyanov, Vadim Lebedev, Andrea Vedaldi, and Victor S Lempitsky. Texture networks: Feed-forward synthesis of textures and stylized images. In *Proceedings of the Con-*

- ference on International Conference on Machine Learning*, volume 1, page 4, 2016. 5
- [55] Liao Wang, Jiakai Zhang, Xinhang Liu, Fuqiang Zhao, Yan-shun Zhang, Yingliang Zhang, Minye Wu, Jingyi Yu, and Lan Xu. Fourier plencotrees for dynamic radiance field rendering in real-time. In *Proceedings of the IEEE/CVF Conference on Computer Vision and Pattern Recognition*, pages 13524–13534, 2022. 3
- [56] Chung-Yi Weng, Brian Curless, Pratul P Srinivasan, Jonathan T Barron, and Ira Kemelmacher-Shlizerman. Humannerf: Free-viewpoint rendering of moving people from monocular video. In *Proceedings of the IEEE/CVF Conference on Computer Vision and Pattern Recognition*, pages 16210–16220, 2022. 3
- [57] Minye Wu, Yuehao Wang, Qiang Hu, and Jingyi Yu. Multi-view neural human rendering. In *Proceedings of the IEEE/CVF Conference on Computer Vision and Pattern Recognition*, pages 1682–1691, 2020. 2
- [58] Fanbo Xiang, Zexiang Xu, Milos Hasan, Yannick Hold-Geoffroy, Kalyan Sunkavalli, and Hao Su. Neutex: Neural texture mapping for volumetric neural rendering. In *Proceedings of the IEEE/CVF Conference on Computer Vision and Pattern Recognition*, pages 7119–7128, 2021. 2
- [59] Hongyi Xu, Thiemo Alldieck, and Cristian Sminchisescu. H-nerf: Neural radiance fields for rendering and temporal reconstruction of humans in motion. *Advances in Neural Information Processing Systems*, 34, 2021. 3
- [60] Alex Yu, Ruilong Li, Matthew Tancik, Hao Li, Ren Ng, and Angjoo Kanazawa. Plencotrees for real-time rendering of neural radiance fields. In *Proceedings of the IEEE/CVF International Conference on Computer Vision*, pages 5752–5761, 2021. 2
- [61] Tao Yu, Zerong Zheng, Kaiwen Guo, Pengpeng Liu, Qionghai Dai, and Yebin Liu. Function4d: Real-time human volumetric capture from very sparse consumer rgb-d sensors. In *Proceedings of the IEEE/CVF Conference on Computer Vision and Pattern Recognition*, pages 5746–5756, 2021. 3
- [62] Jiakai Zhang, Xinhang Liu, Xinyi Ye, Fuqiang Zhao, Yan-shun Zhang, Minye Wu, Yingliang Zhang, Lan Xu, and Jingyi Yu. Editable free-viewpoint video using a layered neural representation. *ACM Transactions on Graphics (TOG)*, 40(4):1–18, 2021. 3
- [63] Richard Zhang, Phillip Isola, Alexei A Efros, Eli Shechtman, and Oliver Wang. The unreasonable effectiveness of deep features as a perceptual metric. In *Proceedings of the IEEE/CVF Conference on Computer Vision and Pattern Recognition*, 2018. 6, 7